

MASTER

A viscoelastic skin model

Jansen, M.Y.

Award date:
1996

[Link to publication](#)

Disclaimer

This document contains a student thesis (bachelor's or master's), as authored by a student at Eindhoven University of Technology. Student theses are made available in the TU/e repository upon obtaining the required degree. The grade received is not published on the document as presented in the repository. The required complexity or quality of research of student theses may vary by program, and the required minimum study period may vary in duration.

General rights

Copyright and moral rights for the publications made accessible in the public portal are retained by the authors and/or other copyright owners and it is a condition of accessing publications that users recognise and abide by the legal requirements associated with these rights.

- Users may download and print one copy of any publication from the public portal for the purpose of private study or research.
- You may not further distribute the material or use it for any profit-making activity or commercial gain

Take down policy

If you believe that this document breaches copyright please contact us providing details, and we will remove access to the work immediately and investigate your claim.

Master of Science Thesis
Eindhoven University of Technology
Faculty of Mechanical Engineering
Division of Computational and Experimental Mechanics

A viscoelastic skin model

M.Y. Jansen

WFW report 96.078
June 1996

Research carried out from September 1995 to June 1996 at
Personal Care Institute, Philips Research Laboratories Eindhoven
Commissioned by Prof. dr. ir. J.D. Janssen (EUT)
Under supervision of Dr. ir. F.J.M. Starmans (Philips),
Dr. ir. C.W.J. Oomens (EUT) and Dr. ir. L.F.A. Douven (Philips)

Abstract

At Philips Nat.Lab., research is done on the primary function of products for personal care by the Personal Care Institute. The main part of the products are apparatus that interact with skin, like shaving and epilating devices. For a better understanding of this interaction simulations are performed with the aid of the finite element method. element method, are important. For realistic simulations an adequate constitutive model of skin is required.

The isotropic incompressible hyperelastic constitutive model that has been used before is in certain cases too limited. As refinements of this model anisotropy and viscosity seem most important. In this project a start is made with the viscoelastic modelling of skin. Therefore a viscous part was added to the current hyperelastic model.

Elastic and viscoelastic parameters were estimated from tensile tests. The estimated parameters were verified with indentation tests. This method was applied to an artificial skin, consisting of two layers and to human skin divided in two layers. With the estimated skin parameters a simulation of a Lady-shave moving along human skin was performed.

Notation

a	scalar
\underline{a}	column of scalars
\tilde{a}	vector
\underline{A}	matrix
\underline{A}^T	transpose of matrix
\underline{A}^{-1}	inverse of matrix
\underline{I}	unit matrix
\mathbf{A}	second order tensor
\mathbf{A}^c	conjugate of tensor
\mathbf{A}^{-1}	inverse of tensor
\mathbf{I}	unit tensor
$E(a)$	expected value of a
\hat{a}	estimate of a
$\tilde{\hat{a}}$	column of estimates a

Contents

Abstract	i
Notation	iii
1 Introduction	1
2 Skin	2
2.1 Structure	2
2.2 Mechanical behaviour	3
2.3 Artificial skin	5
3 Model and parameters	6
3.1 Model	6
3.1.1 Constitutive principles	6
3.1.2 Hyperelasticity	7
3.1.3 Viscoelasticity	8
3.2 Model parameters	10
4 Experiments	13
4.1 Tensile test	13
4.1.1 Experimental set-up	14
4.1.2 Experimental results	14
4.2 Indentation test	15
4.2.1 Experimental set-up	15
4.2.2 Experimental results	16
5 Numerical results	20
5.1 Parameter estimation	20
5.1.1 Parameter estimation tool	20
5.1.2 Estimation with elastic model	21
5.1.3 Estimation with viscoelastic model	24
5.2 Experiment simulation	27
5.2.1 Simulation set-up	27
5.2.2 Simulation results	28

6	An application	33
6.1	Simulation set-up	33
6.2	Simulation results	34
7	Conclusions and recommendations	37
7.1	Conclusions	37
7.2	Recommendations	38
A	The Piola-Kirchoff stress	43
A.1	The elastic Piola-Kirchoff stress	43
A.2	The viscoelastic Piola-Kirchoff stress	44
B	Parfit	45
B.1	File <code>trek_vm.c</code>	45

Chapter 1

Introduction

At Philips Nat.Lab., research is done on the primary function of products for personal care by the Personal Care Institute. The main part of the products are apparatus that interact with skin, like shaving and epilating devices. For a better understanding of this interaction both experimental research, mainly in vivo, as well as model study, with the aid of the finite element method, are important. For realistic simulations an adequate constitutive model of skin is required.

The isotropic incompressible hyperelastic constitutive model that has been used before is in certain cases too limited. As refinements of this model anisotropy and viscosity seem most important. The anisotropic behaviour of skin finds expression when skin is stretched in different directions. Viscous behaviour is found when for example a constant indentation force is applied, in which case the skin shows creep. This time dependent behaviour is important when a shaving system moves along the skin.

In this project a start is made with the viscoelastic modelling of skin. The anisotropic behaviour of skin is not considered here, it is dealt with in an other project.

The main target of this project is to develop an appropriate model for the viscoelastic properties of skin at large deformations and compare it with the current hyperelastic model. To determine the parameters of the models experiments are required. Skin is a complex material and experimenting on skin is not easy. To avoid difficulties at first it is started with modelling of and experimenting on an artificial skin, which consists of two layers. When it follows that this is an adequate method for modelling, a start can be made with modelling in vivo skin.

Chapter 2 starts with a short review about the structure of skin, its mechanical behaviour and the construction of the artificial skin that is used for the experiments performed. The constitutive models used and the method for estimating the parameters of these models are discussed in Chapter 3. The experimental set-up and the experimental results of a tension test, performed on the separate layers of the artificial skin and an indentation test, performed on the artificial skin, its separate layers and human skin are described in Chapter 4. In Chapter 5 the set-up and results of the parameter estimations and indentation test simulations are given. These results are also discussed there. A simulation of a shaving system moving along a leg, with the parameters estimated for the skin model, is described in Chapter 6. In Chapter 7 conclusions are drawn and recommendations are made.

Chapter 2

Skin

This chapter starts with a section about the structure of skin. In Section 2.2 its mechanical behaviour is discussed and the last section describes the construction of the artificial skin, used for experiments.

2.1 Structure

The skin has a stratified structure consisting of two main layers: the epidermis and the dermis (Figure 2.1).

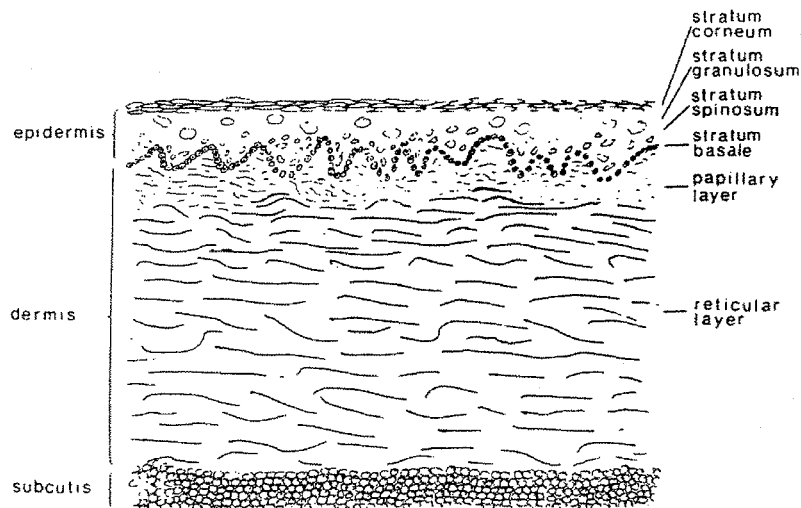


Figure 2.1: The skin

The epidermis is the outer layer of the skin. A continuous reproduction of epithelial cells at the boundary with the dermis causes migration towards the external surface. The cells keratinize as they migrate. The epidermis can generally be divided in four strata. Each stratum consists of cells that are in the same phase of keratinisation. The outer layer of the

epidermis is the stratum corneum. This stratum consists of death keratinized cells and is in general between 0.008 and 0.013 mm thick, except for the sole of the foot and the palm of the hand, on which the stratum corneum has a thickness up to 1.4 mm. In general the thickness of the complete epidermis varies between body sites from 0.07 to 0.12 mm.

The dermis supports the epidermis. It consists mainly of a dense network of three fibrous proteins: collagen, elastin and reticulin. This network is permeated by a semigel matrix of ground substance, which consists of among others water, polysaccharides, proteins and enzymes. In this main structure there are a lot of irregularities, like blood vessels, lymph vessels, hair follicles, sweat glands, nerve endings, and small hair muscles. The thickness of the dermis varies between body sites from 0.3 to 4 mm.

At the inner side the skin is bounded by a fatty layer, which is named the subcutis or hypodermis.

2.2 Mechanical behaviour

Still there is a lot of discussion about the influence of the stratum corneum on the mechanical properties of the epidermis. According to [Chris 77] the stratum corneum dominates the mechanical properties of the epidermis, because of its relative low elasticity.

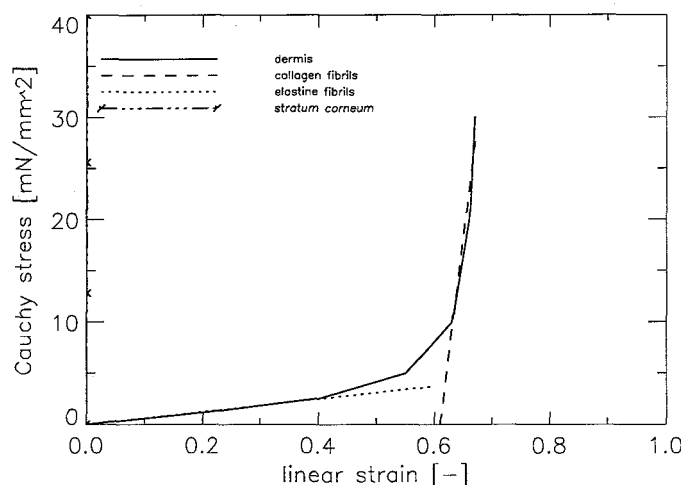


Figure 2.2: The tensile characteristics of dermis measured by [Daly 82] and the stratum corneum, measured by [Wild 71], where the linear strain is the fraction of the length change and the reference length

[Wild 71] measured tensile curves of the stratum corneum at 32 % RH and 76 % RH at 30 °C (± 1 °C). To obtain a tensile characteristic at a quite normal relative humidity of 54 %, it was interpolated between the linear parts of the measured curves. When it is assumed that the stratum corneum thickness is 0.010 mm, for the Young's modulus follows $64 \cdot 10^6$ Pa.

Besides elastic behaviour it also shows dissipative behaviour. In dry stratum corneum the viscous effect is small compared to that of the dermis [Chris 77]. The elasticity, brittleness and dissipation are strongly dependent on the humidity of the stratum corneum. It becomes less stiff, less brittle and more dissipative when the humidity increases [Chris 77, ParkII 72].

Because other layers of the epidermis contain living cells as the dermis does, it is expected that its mechanical behaviour is similar to that of the dermis.

During a tensile test, the dermis will be weak at low strains (see Figure 2.2, Young's modulus $\approx 5 \cdot 10^3 Pa$ [Daly 82]). In this stage, mainly elastine fibres are involved, while the collagen fibre network is straightening out. Collagen properties dominate the dermis' behaviour when their fibres are straightened. In contrast to elastine fibres, the collagen fibres are stiff (Young's modulus $\approx 1.8 \cdot 10^5 Pa$).

Besides elastic behaviour the dermis exhibits also viscous behaviour. This can be concluded from results of a tensile relaxation test, [Daly 82]. In Figure 2.3 it is shown that the dermis only shows time dependent behaviour at large strains (> 0.40) during a tensile test. At these large strains the collagen fibres dominate the mechanical properties and so it can be concluded that they behave viscoelastic. At lower strains like 0.35 when mainly elastine fibres are involved, no relaxation occurs. However, studies on the mechanical properties of tendon [Minns 73, Hool 80], which has a lot of similarities with skin in structure and composition, suggest that besides collagen fibrils also the ground substance contributes to the time dependent behaviour.

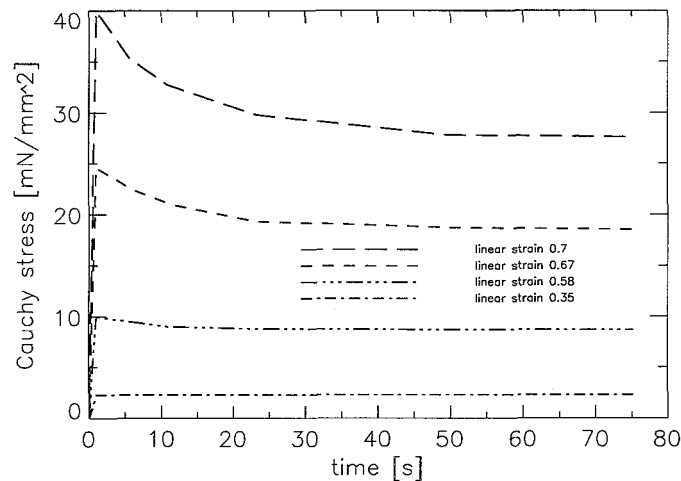


Figure 2.3: The tensile relaxation characteristics of dermis at various linear strain levels, measured by [Daly 82]

Compared to the dermis the stratum corneum has a very large Young's modulus, but its layer thickness is much smaller. To determine whether the stratum corneum has a large effect on the mechanical properties of human skin, a measure for the stiffness, layer thickness * Young's modulus, is calculated. This layer 'stiffness' is restored in table 2.2, where for the layer thickness an average value is taken. The calculated measure for the stiffness of the stratum corneum seem to have the same order as the 'stiffness' of the collagen part of the dermis and is about 100 times stiffer than the elastine part of the dermis. So it can be concluded from this that the stratum corneum layer must play a role in the mechanical behaviour of the skin.

The subcutis protects the skin against impact forces by absorbing energy. In less extreme load cases this energy dissipation is hardly observed and the force is equally divided along this layer [North 78].

	layer thickness [m]	Young's modulus [Pa]	'stiffness' [N/m]
stratum corneum	$1 \cdot 10^{-5}$	$6 \cdot 10^7$	$6 \cdot 10^2$
dermis	$1 \cdot 10^{-3}$		
elastine part		$5 \cdot 10^3$	5
collagen part		$2 \cdot 10^5$	$2 \cdot 10^2$

Table 2.1: A measure for the layer stiffness of the stratum corneum and the dermis, layer thickness \cdot Young's modulus

In general the skin can be considered as a stratified material with a stiff elastic top layer, the stratum corneum and a soft viscoelastic basic layer, the dermis and the epidermis without stratum corneum.

2.3 Artificial skin

In vivo testing causes many problems. One has to deal with body movements, limited time and nondestructive testing. Experiments on skin show its inhomogeneous behaviour and large variations between persons and body sites. In vitro testing expands the possibilities, but still one has to handle possible inhomogeneities, poor reproducibility and degradation problems. Cultivated skin is still not far enough developed. Its mechanical properties are not yet comparable to those of human skin. For testing a method an artificial skin can be useful. It does not have the specific problems of a living tissue. An important condition is that the mechanical properties on which is focussed must be comparable to those of human skin.

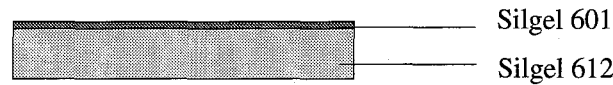


Figure 2.4: Cross-section of the artificial skin used for experiments

So at first instance it is decided to start with experimenting on an artificial skin to avoid the various problems that appear with in vivo and in vitro testing. Considering nonbiological materials for a physical model, it shows that soft rubber gels are nonlinear, viscoelastic and can bear large deformations like skin. Ignoring the anisotropic properties of skin, soft rubbers are useful as a model material.

Analogous to skin, artificial skin can be build up of various layers. Initially a model of two layers is chosen [Jans 95]: a stiff elastic top layer simulating the stratum corneum and a soft viscoelastic basic layer simulating the dermis and the epidermis without stratum corneum.

For the experiments described in the sequel, the bottom layer was produced of a sticky soft viscoelastic silicon rubber S612 (Silgel 612 of Wacker Chemicals with mix ratio=basic component:harder=a:b=1:1, thickness 2.5 mm) and S601 (Silgel 601 of Wacker Chemicals with mix ratio=a:b=9:1, thickness 0.82 mm) was used for the top layer. This is a stiffer, elastic and not sticky silicon rubber.

Chapter 3

Model and parameters

The constitutive models used for simulations are described in Section 3.1. In Section 3.2 the method for estimating parameters of these models from experiments is explained.

3.1 Model

During shaving and epilating processes large deformations may occur. At these deformations skin shows nonlinear anisotropic viscoelastic behaviour. So for realistic simulations the constitutive model should be able to handle this behaviour. As indicated previously the anisotropic behaviour is left out of consideration here.

For practical reasons the constitutive models that are available within the finite element package MARC are employed in this study. A hyperelastic model seems to be a good option for the elastic part of the constitutive model. This nonlinear incompressible description, originally formulated to model vulcanised rubbers, is described in Section 3.1.2. Section 3.1.3 gives the extension of the hyperelastic model with viscous behaviour, but first the most important constitutive principles supporting the logic of the constitutive models are described in Section 3.1.1.

3.1.1 Constitutive principles

Constitutive behaviour involves behaviour of material that can not be described by the general physical laws only, it is material dependent.

General equations for constitutive behaviour are derived with the use of the thermodynamic balance laws, preservation of mass, preservation of momentum, preservation of moment of momentum and other restrictions. These general equations can be simplified as consequence of restricting physical principles. Some restrictions are general and apply to all materials, like the principle of determinism, local action and the objectivity. Other are material dependent due to for example symmetries of crystal structures, incompressibility and the presence of fibres. Some important restricting principles used in the sequel are shortly described here:

Determinism The Cauchy stress σ in a certain instantaneous state is determined uniquely by the total history of the current position \vec{x} of all material points of the continuum.

Local action The Cauchy stress σ in a certain instantaneous state, in a material point is determined by the total history of the position \vec{x} in the immediate surrounding. This

means that only the history of the local deformation tensor \mathbf{F} enters the constitutive equation. \mathbf{F} is defined from the current position \vec{x} and the reference position \vec{x}_0 by: $d\vec{x} = \mathbf{F} \cdot d\vec{x}_0$ with $d\vec{x}$ and $d\vec{x}_0$ infinitesimal position difference vectors.

Objectivity The constitutive relationship will not change when a rigid translation or a rigid rotation or both are applied to the observer of a continuum when objective or invariant quantities are used. The Cauchy stress $\boldsymbol{\sigma}$ and the left Cauchy-Green strain tensor $\mathbf{B} = \mathbf{F} \cdot \mathbf{F}^c$ are objective quantities. Invariant variables are not sensitive to coordinate transformations for example the second Piola-Kirchoff stress $\mathbf{S} = j\mathbf{F}^{-1} \cdot \boldsymbol{\sigma} \cdot \mathbf{F}^{-c}$, in which $j = \det(\mathbf{F})$, and the right Cauchy-Green strain tensor $\mathbf{C} = \mathbf{F}^c \cdot \mathbf{F}$.

Hidden variables The use of hidden variables enables reformulation in current variables, letting the hidden variables take account for time history in certain extent. In case of hyperelasticity as described in Section 3.1.2 no hidden variables are needed as only the current strain state plays a role in the stresses. The viscoelastic model of Section 3.1.3 is deduced by means of one hidden tensorial variable \mathbf{Q} .

The resulting models will be theoretically well-based. Their usefulness however for describing the behaviour of some material can only be determined by experiments.

3.1.2 Hyperelasticity

It is started from the local isothermal Clausius-Duhem inequality (Equation 3.1) which should hold for all thermodynamically allowed processes i.e. which obey the balance of mass, momentum, moment of momentum and energy.

$$\rho_0 \dot{\Psi} - \mathbf{S} : \dot{\mathbf{E}} \leq 0 \quad (3.1)$$

Here the $(\dot{})$ indicates the material time derivative. Furthermore Ψ is the Helmholtz free energy, ρ_0 the mass density in a chosen reference state at reference time t_0 and \mathbf{E} the Green-Lagrange strain tensor, which is defined as:

$$\mathbf{E} = \frac{1}{2}(\mathbf{C} - \mathbf{I}) \quad (3.2)$$

To derive an elastic model it is assumed that the Helmholtz free energy Ψ and the second Piola-Kirchoff stress tensor \mathbf{S} only depend on the current strain state characterised by the Green-Lagrange strain tensor \mathbf{E} . From the demand that the equality in Equation 3.1 should hold for all allowed \mathbf{E} , it follows for \mathbf{S} :

$$\mathbf{S} = \rho_0 \frac{\partial \Psi}{\partial \mathbf{E}} \quad (3.3)$$

Volume strain and deformation strain can be made explicit by splitting up the free energy according to [Simo 87]:

$$\Psi = U^0(j) + \bar{\Psi}^0(\bar{\mathbf{E}}) \quad (3.4)$$

in which U^0 is the specific energy due to volume (or axiatic) strain and $\bar{\Psi}^0$ is the Helmholtz free energy due to deformational (or isochoric) strain. The isochoric part of the Green-Lagrange strain $\bar{\mathbf{E}}$ is defined as:

$$\bar{\mathbf{E}} = \frac{1}{2}(\bar{\mathbf{F}}^c \cdot \bar{\mathbf{F}} - \mathbf{I}) \quad (3.5)$$

where the isochoric deformation tensor $\bar{\mathbf{F}}$ is defined as:

$$\bar{\mathbf{F}} = j^{-\frac{1}{3}} \mathbf{F} \quad (3.6)$$

Note that $\det(\bar{\mathbf{F}}) = 1$ for all arbitrary \mathbf{F} . By substituting Equation 3.4 in Equation 3.3 and elaborate to j and $\bar{\mathbf{E}}$ as described in Appendix A, it follows for the second Piola-Kirchoff stress tensor:

$$\mathbf{S} = \rho_0 j \frac{\partial U^0}{\partial j} \mathbf{C}^{-1} + \rho_0 j^{-\frac{2}{3}} \frac{\partial \bar{\Psi}^0}{\partial \bar{\mathbf{E}}} : \left({}^4\mathbf{I} - \frac{1}{3} \mathbf{C} \mathbf{C}^{-1} \right) \quad (3.7)$$

with ${}^4\mathbf{I}$ the fourth order identity tensor and $\mathbf{C} \mathbf{C}^{-1}$ the dyadic product of the right Cauchy-Green strain tensor \mathbf{C} and its inverse \mathbf{C}^{-1} . In case of incompressible material behaviour $j = 1$, Equation 3.7 can be reformulated to:

$$\mathbf{S} = \rho_0 p \mathbf{C}^{-1} + \rho_0 \frac{\partial \bar{\Psi}^0}{\partial \bar{\mathbf{E}}} : \left({}^4\mathbf{I} - \frac{1}{3} \mathbf{C} \mathbf{C}^{-1} \right) \quad (3.8)$$

with the hydrostatic pressure p as independent state variable. The Cauchy stress can be calculated by:

$$\boldsymbol{\sigma} = \frac{1}{j} \mathbf{F} \cdot \mathbf{S} \cdot \mathbf{F}^c \quad (3.9)$$

Mooney-Rivlin material

The elastic Mooney-Rivlin model uses a specific choice for the strain energy function Ψ defined by:

$$\Psi = \frac{1}{\rho_0} [C_{10}(i_1 - 3) + C_{01}(i_2 - 3)] \quad (3.10)$$

in which C_{10} and C_{01} are two material parameters and $i_1 = \text{tr}(\mathbf{C})$ and $i_2 = \frac{1}{2}((\text{tr}(\mathbf{C}))^2 - \text{tr}(\mathbf{C}^2))$ are the first and the second invariant of the right Cauchy-Green tensor \mathbf{C} . The third invariant $i_3 = \det(\mathbf{C})$ is equal to one, because of the supposed incompressibility.

The first order Mooney-Rivlin model can be expanded to a third order model, considered by Jamus, Green and Simpson, and implemented in the MARC program. This expanded Mooney-Rivlin model is given in Equation 3.11.

$$\Psi = \frac{1}{\rho_0} [C_{10}(i_1 - 3) + C_{01}(i_2 - 3) + C_{11}(i_1 - 3)(i_2 - 3) + C_{20}(i_1 - 3)^2 + C_{30}(i_1 - 3)^3] \quad (3.11)$$

3.1.3 Viscoelasticity

For the viscoelastic description according to [Simo 87], a viscous part is added to the strain energy function of Equation 3.4, with the viscous isochoric part $-\mathbf{Q} : \bar{\mathbf{E}}$ and the viscous volumetric part $\Psi_I(\mathbf{Q})$.

$$\Psi(\mathbf{E}, \mathbf{Q}) = U^0(j) + \bar{\Psi}^0(\bar{\mathbf{E}}) - \mathbf{Q} : \bar{\mathbf{E}} + \Psi_I(\mathbf{Q}) \quad (3.12)$$

The internal variable \mathbf{Q} is used for modelling the viscous part by taking the materials' fading history in account. The second Piola-Kirchoff stress can be obtained by substituting Equation

3.12 into Equation 3.1 and elaborate for arbitrary deformations. Assuming $\mathbf{S} = \mathbf{S}(\mathbf{C}, \mathbf{Q})$ with \mathbf{C} and \mathbf{Q} at the current time point (see Appendix A), the next equation can be obtained.

$$\mathbf{S} = \rho_0 j \frac{\partial U}{\partial j} \mathbf{C}^{-1} + \rho_0 j^{-\frac{2}{3}} \frac{\partial \bar{\Psi}^0}{\partial \bar{\mathbf{E}}} : (\mathbf{I} - \frac{1}{3} \mathbf{C} \mathbf{C}^{-1}) - \rho_0 j^{-\frac{2}{3}} \mathbf{Q} : (\mathbf{I} - \frac{1}{3} \mathbf{C} \mathbf{C}^{-1}) \quad (3.13)$$

Equation 3.13 can be simplified for an incompressible standard linear solid with $j = 1$, hydrostatic pressure p and with one internal variable $\mathbf{Q} = \mathbf{q}$ to

$$\mathbf{S} = -\rho_0 p \mathbf{C}^{-1} + \rho_0 \frac{\partial \bar{\Psi}^0}{\partial \bar{\mathbf{E}}} : (\mathbf{I} - \frac{1}{3} \mathbf{C} \mathbf{C}^{-1}) - \rho_0 \mathbf{q} : (\mathbf{I} - \frac{1}{3} \mathbf{C} \mathbf{C}^{-1}) \quad (3.14)$$

A standard linear solid applies the following linear rate equation in which ν is the single relaxation time and γ gives the energy function multiplier.

$$\dot{\mathbf{q}} + \frac{1}{\nu} \mathbf{q} = \frac{1 - \gamma}{\nu} \frac{\partial \bar{\Psi}^0(\bar{\mathbf{E}})}{\partial \bar{\mathbf{E}}} : (\mathbf{I} - \frac{1}{3} \mathbf{C} \mathbf{C}^{-1}), \quad \mathbf{q}|_{t=0} = \mathbf{0} \quad (3.15)$$

Where $\mathbf{I} - \frac{1}{3} \mathbf{C} \mathbf{C}^{-1}$ extracts the isochoric part from $\partial \bar{\Psi}^0(\bar{\mathbf{E}})/\partial \bar{\mathbf{E}}$, like in Equation 3.7. This differential equation can also be formulated in an integral formulation:

$$\mathbf{q} = (1 - \gamma) \left[\frac{\partial \bar{\Psi}^0(\bar{\mathbf{E}})}{\partial \bar{\mathbf{E}}} - \frac{\partial \bar{\Psi}^0(\bar{\mathbf{E}})}{\partial \bar{\mathbf{E}}} \Big|_{t=0} e^{-\frac{t}{\nu}} - \int_{\tau=0}^t \frac{d}{d\tau} \left(\frac{\partial \bar{\Psi}^0(\bar{\mathbf{E}})}{\partial \bar{\mathbf{E}}} \right) e^{-\frac{t-\tau}{\nu}} d\tau \right] \quad (3.16)$$

A standard linear solid can be schematically represented by a Kelvin element in series with a spring as drawn in Figure 3.1. The constants for the springs and dashpot are given in this figure, assuming that the spring in series has a spring constant of k . The tensions on the elements are also given where $\sigma^0 = \partial \bar{\Psi}^0/\partial \bar{\mathbf{E}}$.

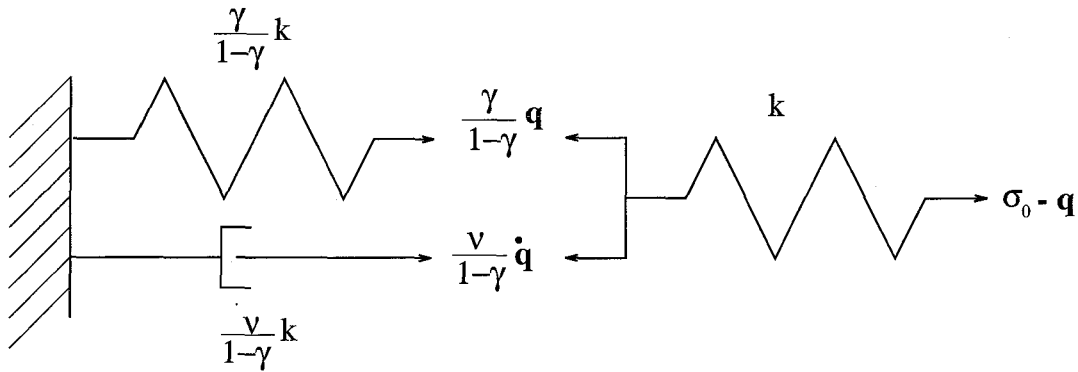


Figure 3.1: A standard linear solid with the stresses and the spring and dashpot constants

A stress relaxation test can be applied to a tie rod with standard linear solid behaviour. The influence of the multiplier γ is drawn in Figure 3.2. When γ becomes larger the final stress and the stress peak become lower.

When the relaxation time ν (see Figure 3.3) is short compared to the point of time, the material does not 'feel' the presence of the dashpot of Figure 3.1 and there remains a system

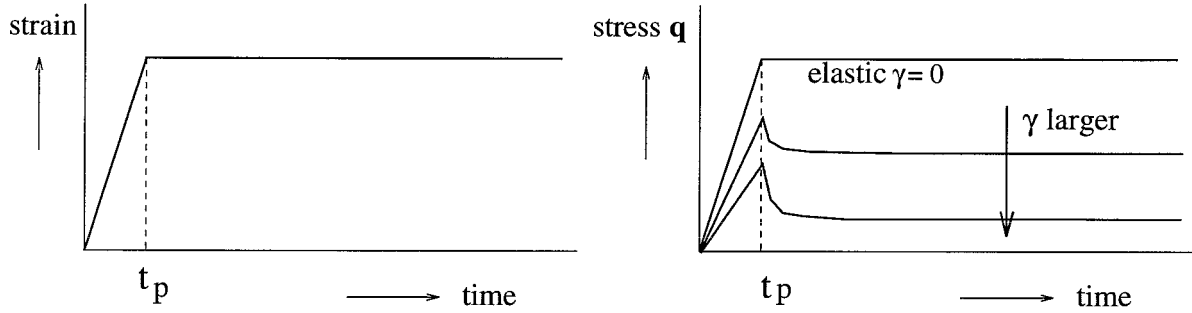


Figure 3.2: The influence of the multiplier γ in a uniaxial relaxation test applied on standard linear solid material

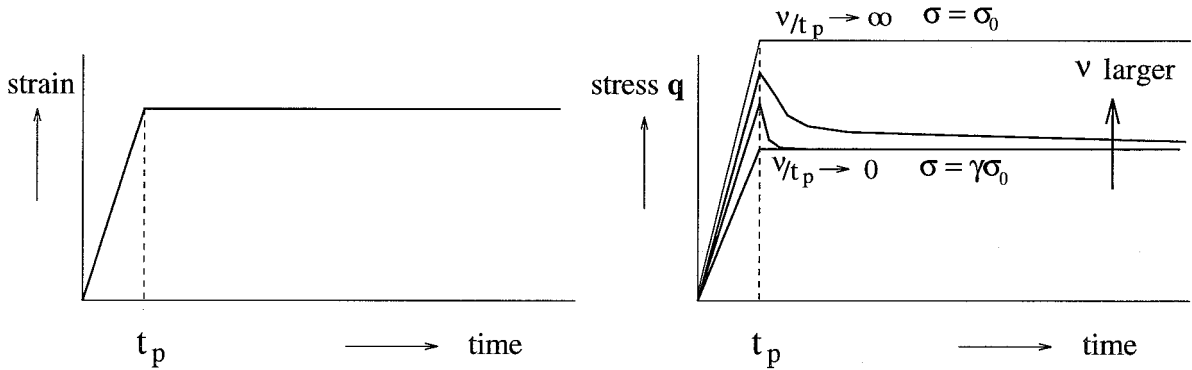


Figure 3.3: The influence of the relaxation time ν in a uniaxial relaxation test applied on standard linear solid material

of two springs, that is soft elastic with stress $\sigma = \gamma\sigma_0$. If ν is very large the dashpot of Figure 3.1 acts rigid. The spring parallel to this dashpot cannot elongate and the material behaviour is only determined by the series spring, which is stiff elastic with stress $\sigma = \sigma_0$. So this material behaves stiff elastic when it has an infinite long relaxation time and when it has a relaxation time of zero it behaves soft elastic. Between these extremes a clear recognizable relaxation curve is observed.

This model for a standard linear solid with one relaxation time can be generalized to a model with more relaxation times. For each added relaxation time a kelvin element with relaxation time ν_α and an energy function multiplier γ_α , is added in series to the standard linear solid of Figure 3.1.

3.2 Model parameters

When measurements are done, observational data errors will always occur. The exact values of these errors are generally not known. So it is impossible to calculate the true values of quantities of interest from these observed values. Different methods are available to estimate

the unknown values. In this section the minimum variance estimator for sequential estimating is described. This method will be employed in Chapter 5.

Sequential parameter estimation

Various methods of estimation take all observed data into account at once. However, it may be advantageous or even necessary to use parts of the available observational data in sequential steps, e.g. in nonlinear cases an iterative solution procedure is necessary. This procedure can be combined with a sequential estimation method.

Assume that m observational data are gathered in the column matrix \tilde{z} . They are equal to m observational quantities h that are supposed to be functions of n quantities or parameters x , of which the true values x_t are to be determined, and m observational errors \tilde{v} .

$$\tilde{z} = h(\tilde{x}_t, \tilde{v}) \quad (3.17)$$

Generally it is supposed that in Equation 3.17 the observational errors can be written separately:

$$\tilde{z} = h(\tilde{x}_t) + \tilde{v} \quad (3.18)$$

For sequential estimating at step $k+1$ Equation 3.18 can be rewritten as:

$$\tilde{z}_{k+1} = h_{k+1}(\tilde{x}_t) + \tilde{v}_{k+1} \quad (3.19)$$

Before proceeding with this expression more information is needed on \tilde{v}_{k+1} . For lack of knowledge assumptions are made for the observational errors. It is assumed that the expected value of the observational errors equals $E(\tilde{v}_{k+1}) = 0$ and their covariance matrix equals $E(\tilde{v}_{k+1} \tilde{v}_{k+1}^T) = \mathbf{R}_{k+1}$.

From the measurement data the values of interest \tilde{x} can be estimated. The estimate $\hat{\tilde{x}}$ is described as the summation of the true value \tilde{x}_t and the estimation error \tilde{w} , which can be described as:

$$\hat{\tilde{x}} = \tilde{x}_t + \tilde{w} \quad (3.20)$$

At step k the estimate $\hat{\tilde{x}}_k$ is written as:

$$\hat{\tilde{x}}_k = \tilde{x}_t + \tilde{w}_k \quad (3.21)$$

It is assumed that the expected value of the estimation errors equals $E(\tilde{w}_k) = 0$ and their covariance $E(\tilde{w}_k \tilde{w}_k^T) = \mathbf{P}_k$. Besides it is supposed that the estimation errors and the observational errors are uncorrelated $E(\tilde{w}_k \tilde{v}_{k+1}^T) = 0$.

Equation 3.19 can be approximated if $\hat{\tilde{x}}_k$ is already close to \tilde{x}_t by:

$$\tilde{z}_{k+1} \approx h_{k+1}(\hat{\tilde{x}}_k) + \mathbf{H}_{k+1}(\hat{\tilde{x}}_k) \delta \tilde{x}_k + \tilde{v}_{k+1} \quad (3.22)$$

with the difference column $\delta \tilde{x}_k = \tilde{x}_t - \hat{\tilde{x}}_k$ and $\mathbf{H}_{k+1}(\hat{\tilde{x}}_k) = \partial h_{k+1}(\tilde{x}) / \partial \tilde{x}^T |_{\tilde{x} = \hat{\tilde{x}}_k}$, the partial derivatives of the nonlinear model to the parameters at $\hat{\tilde{x}}_k$. Rewriting Equation 3.22 using Equation 3.21 a linear model is obtained, in which $\tilde{z}_{k+1} - h_{k+1}(\hat{\tilde{x}}_k)$ are the so-called residuals.

$$\tilde{z}_{k+1} - h_{k+1}(\hat{\tilde{x}}_k) = \mathbf{H}_{k+1}(\hat{\tilde{x}}_k) \delta \tilde{x}_k + \tilde{v}_{k+1}, \quad 0 = \delta \tilde{x}_k + \tilde{w}_k \quad (3.23)$$

The minimum variance estimator $\delta \hat{x}_{\tilde{k}}$ for $\delta x_{\tilde{k}}$ can be derived to be:

$$\delta \hat{x}_{\tilde{k}} = \mathbf{K}_{k+1}(\tilde{z}_{k+1} - h_{k+1}(\hat{x}_{\tilde{k}})) \quad (3.24)$$

with \mathbf{K}_{k+1} the weighting or gain matrix given in the sequel. The new estimation for x_t follows from $\hat{x}_{\tilde{k}+1} = \hat{x}_{\tilde{k}} + \delta \hat{x}_{\tilde{k}}$ in which $\mathbf{K}_{k+1}(\tilde{z}_{k+1} - h_{k+1}(\hat{x}_{\tilde{k}}))$ is the so-called innovation for the new estimate:

$$\hat{x}_{\tilde{k}+1} = \hat{x}_{\tilde{k}} + \mathbf{K}_{k+1}(\tilde{z}_{k+1} - h_{k+1}(\hat{x}_{\tilde{k}})) \quad (3.25)$$

The gain matrix \mathbf{K}_k and the covariance matrix of the estimation errors \mathbf{P}_k need to be updated for each next estimation step.

$$\begin{aligned} \mathbf{K}_k &= \mathbf{P}_k \mathbf{H}_{k+1}^T (\mathbf{R}_{k+1} + h_{k+1} \mathbf{P}_k \mathbf{H}_{k+1}^T)^{-1} \\ \mathbf{P}_{k+1} &= (\mathbf{I} - \mathbf{K}_{k+1} h_{k+1}) \mathbf{P}_k \end{aligned} \quad (3.26)$$

Convergence problems because of a too small or singular \mathbf{P}_k can be avoided by replacing \mathbf{P}_k in Equation A.8 by $\mathbf{P}_k + \mathbf{Q}_k$, where \mathbf{Q}_k is a nonnegative symmetric matrix. The set of equations then becomes:

$$\begin{aligned} \hat{x}_{\tilde{k}+1} &= \hat{x}_{\tilde{k}} + \mathbf{K}_{k+1}(\tilde{z}_{k+1} - h_{k+1}(\hat{x}_{\tilde{k}})) \\ \mathbf{K}_k &= (\mathbf{P}_k + \mathbf{Q}_k) \mathbf{H}_{k+1}^T (\mathbf{R}_{k+1} + h_{k+1}(\mathbf{P}_k + \mathbf{Q}_k) \mathbf{H}_{k+1}^T)^{-1} \\ \mathbf{P}_{k+1} &= (\mathbf{I} - \mathbf{K}_{k+1} h_{k+1})(\mathbf{P}_k + \mathbf{Q}_k) \end{aligned} \quad (3.27)$$

In the estimation program Parfit that is used in the sequel a value for χ^2 is given at every estimation. The χ^2 distribution is a measure for the proportion between the approximated measurement error covariance, calculated with the residuals $\tilde{z}_{k+1} - h_{k+1}(\hat{x}_{\tilde{k}})$ and the given measurement error covariance \mathbf{R}_{k+1} . The χ^2 can be calculated with Equation 3.28 with $v = m - n$ degrees of freedom, in which m is the number of observations and n is the number of parameters.

$$\chi_v^2 = (\tilde{z}_{k+1} - h_{k+1}(\hat{x}_{\tilde{k}}))^T \mathbf{R}_{k+1}^{-1} (\tilde{z}_{k+1} - h_{k+1}(\hat{x}_{\tilde{k}})) \quad (3.28)$$

When χ^2 is known, the standard deviation s of the measurements can be determined. In the sequel for \mathbf{R}_{k+1} is taken $\mathbf{R}_{k+1} = R \cdot \mathbf{I}$ with \mathbf{I} the identity with size m . Therefore the standard deviation s can be calculated with Equation 3.29 supposing that the used model is perfect and so all the deviations are due to measuremental errors.

$$s = \sqrt{\frac{\chi_v^2 R}{v}} \quad (3.29)$$

Chapter 4

Experiments

From tensile tests on the layers of artificial skin and human skin data is obtained to estimate parameters. The tensile tests on the human skin layers were obtained from literature as described in Section 2.2. With the estimated parameters indentation tests are simulated, that are also performed to verify the estimated parameters.

The performed experiments are described in this chapter; the tensile tests on the rubbers in Section 4.1 and the indentation tests on rubbers and human skin in Section 4.2.

4.1 Tensile test

Tensile tests were performed on the separate layers of the artificial skin. In Section 4.1.1 the experimental set-up of the tensile tests is described and in Section 4.1.2 the results of these experiments.

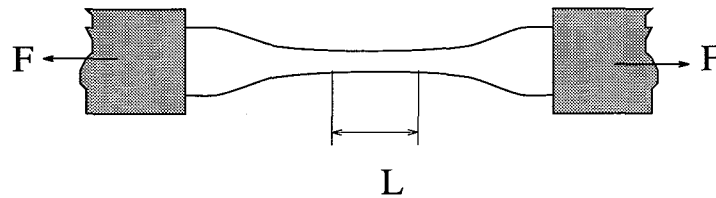


Figure 4.1: Experimental set-up of a tensile test on stiff Silgel 601

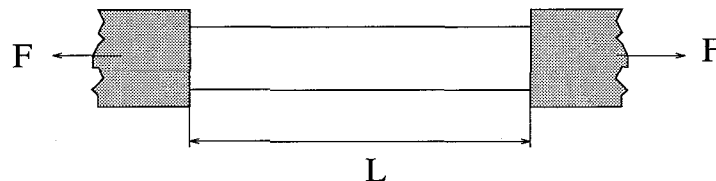


Figure 4.2: Experimental set-up of a tensile test on Silgel 612

4.1.1 Experimental set-up

All tensile tests were performed on the standard stretching device Zwick 1434. Samples of the stiff S601 were obtained casting the mixed basic components in a casting-mould. Testing this material, the range of the force F was 2 N and the displacement range 2 mm . The tie rod thickness was 1.53 mm , the total length between the clamps was 90.1 mm , the width of the measuring area 10 mm and its length $L\ 30\text{ mm}$ (see Figure 4.1). The elongation of the measuring area was raised up to 2 mm . The displacement velocity was coupled to the distance between the clamps. The experiment was repeated several times with the same sample with different velocities, varying from 1.25 mm/min to 40 mm/min .

The samples of soft S612 (see Figure 4.2) were cut from a 1.5 mm thick sheet with a width of 20 mm . The samples were treated with normal fluid toilet soap to avoid sticking during the preparation of the experiments. The measuring length of the vertically placed samples was equal to the distance between the clamps. It varied from sample to sample from 40 to 50 mm . For every measurement a new test sample was used. While stretching the soft viscoelastic S612, the force range was 100 mN and the displacement range 20 mm . In the quasistatic measurement the displacement velocity was 20 mm/min and the final strain was about 0.50 . In the relaxation tests the samples were elongated with a velocity of 200 mm/s until a linear strain of 0.501 and 0.314 was reached. Then the strain remained constant for at least four minutes.

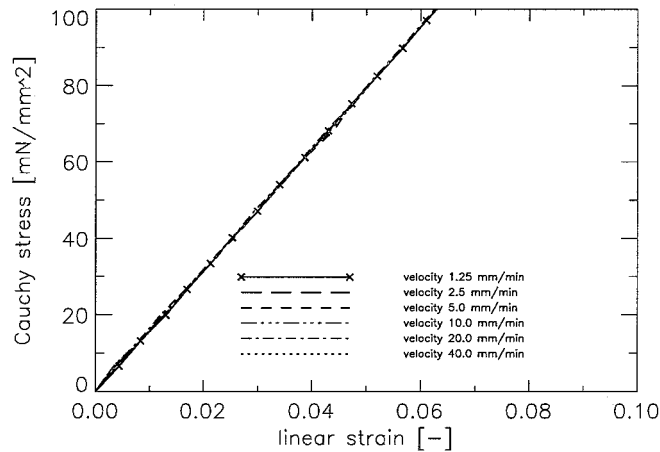


Figure 4.3: Results of tensile test on Silgel 601 using the linear strain (the length change divided by the reference length) as strain

4.1.2 Experimental results

The results of the uniaxial tensile tests on Silgel 601 are plotted in Figure 4.3. The elongation velocity seems to have a negligible influence on the tensile characteristics. No time dependent effect appears in this test.

Results of the tensile test on Silgel 612 are displayed in Figure 4.4. Comparing this figure with Figure 4.3 it can be concluded that Silgel 601 is much stiffer than Silgel 612. The first part of the S612 characteristic (strains < 0.25) seems to be less stiff, which could be caused by sagging of the material before the experiment started.

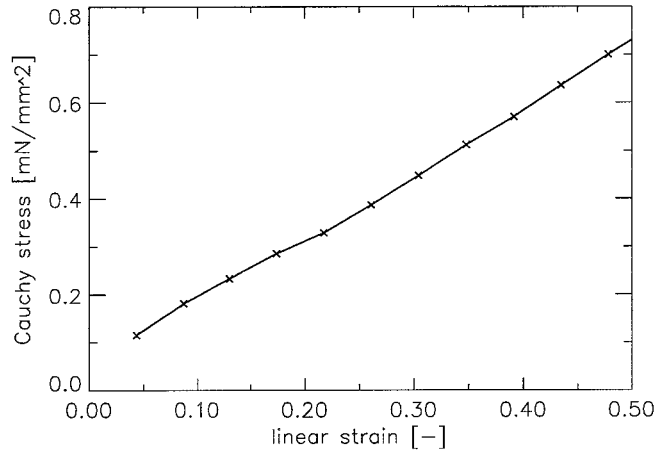


Figure 4.4: Results of tension test on Silgel 612

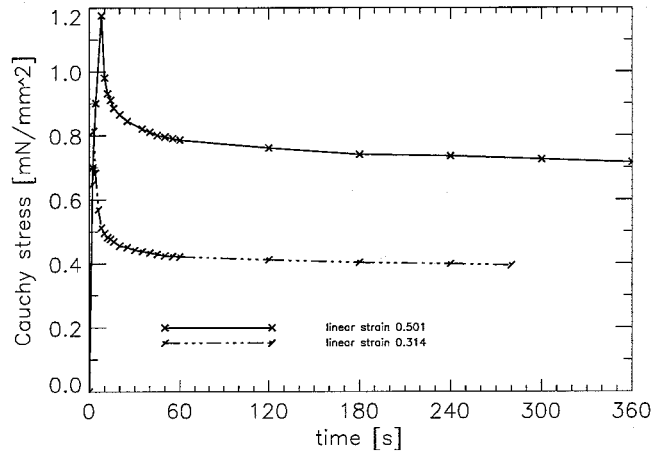


Figure 4.5: Results of relaxation test on a Silgel 612 tie rod

The viscoelastic behaviour of Silgel 612 finds expression in the measured relaxation curves shown in Figure 4.5. After four minutes the material is still relaxing.

4.2 Indentation test

Indentation tests were performed on the artificial skin, its separate layers and human skin. In Section 4.2.1 the measuring equipment and the set-up for the indentation tests are shortly described. In Section 4.2.2 the results of these experiments are presented.

4.2.1 Experimental set-up

The indentation characteristics were measured with the Electro Dynamo Meter (EDM), described by [Vos 88], schematically drawn in Figure 4.6. The EDM was equipped with a spherically shaped probe with a radius of 1.5 mm, fixed on the indentation pin. This indentation pin transduces the generated force. First the probe was positioned just against the surface of the material to define a zero point. This was hard and can have given deviations

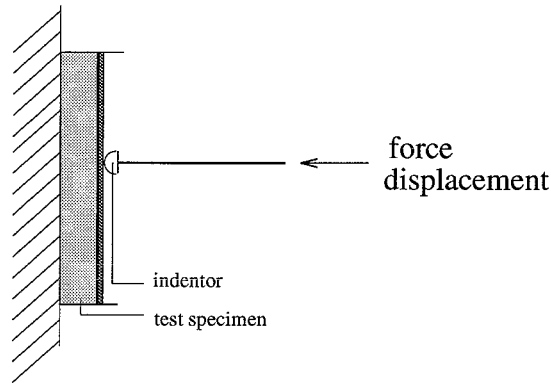


Figure 4.6: Indentation test measuring equipment, the Electro Dynamo Meter

in the displacement measuring. With quasistatic indentation experiments the the first measurement at 0.01 mN was used as zero point. This was not possible for the creep tests and so the position errors could be larger in that kind of measuring. Apart from the positioning errors, the measuring error of the measured displacements was at most 0.01 mm .

Quasistatic measurements and creep tests were performed on Silgel 601 (10 mm thick), Silgel 612 (2.5 and 10.0 mm thick) and on artificial skin (basic layer Silgel 612 2.5 and 10.0 mm thick and a top layer of Silgel 601 0.82 mm thick). All these samples were situated in a plastic cylindrical tray with an internal diameter of 50 mm . The elapsed time between two measuring points of a curve was 15 seconds.

4.2.2 Experimental results

The results of the quasistatic indentation test on Silgel 601 are shown in Figure 4.7 and the creep indentation experiment is monitored in Figure 4.8. Hardly any time dependent effect be distinguished. The indentations in the creep experiments are a little larger than in the quasistatic measuring at the same force. This could be a consequence of poor positioning of the probe before the measurement.

The results of quasistatic indentation of Silgel 612 is displayed in Figure 4.9. This test is performed on two samples; one with thickness 2.5 mm and one with thickness 10.0 mm . The 10 mm thick layer was about 4 times softer than the 2.5 mm thick layer. So the stiffness seem proportional with the layer thickness. The creep test on the 2.5 mm thick layer shows a clear time dependent behaviour (see Figure 4.10).

On artificial skin also a quasistatic indentation test and a creep test were performed. Results of these experiments are displayed in Figure 4.11 and 4.12. From the quasistatic characteristics can be concluded that this artificial skin is much stiffer than the 2.5 mm thick Silgel 612 basic layer itself (compare Figure 4.11 and Figure 4.9).

From the results of the creep experiment (see Figure 4.12) it can be concluded that the artificial skin shows time dependent behaviour that is less clear at low forces. Compared to the creep characteristics of the 2.5 mm thick S612 the artificial skin shows less creep (see Figure 4.10).

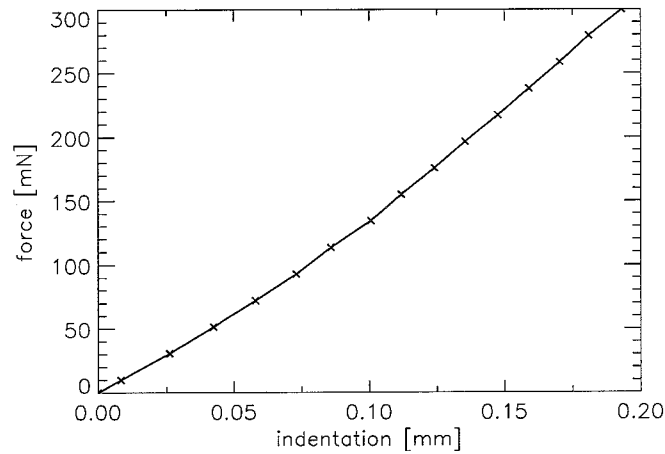


Figure 4.7: Results of quasistatic indentation test on Silgel 601, 10 mm thick

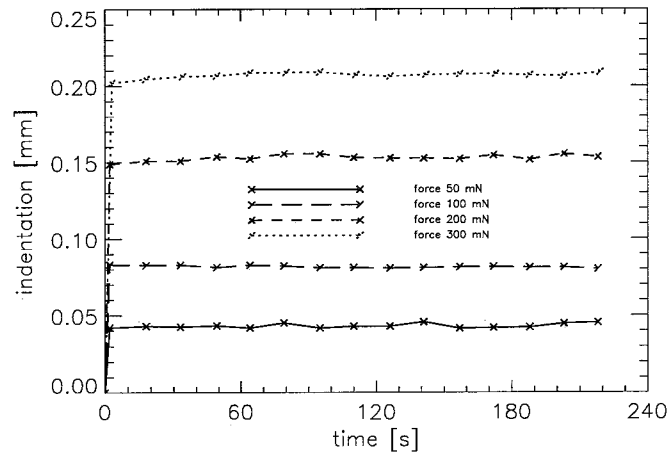


Figure 4.8: Results of creep indentation test on Silgel 601, 10 mm thick

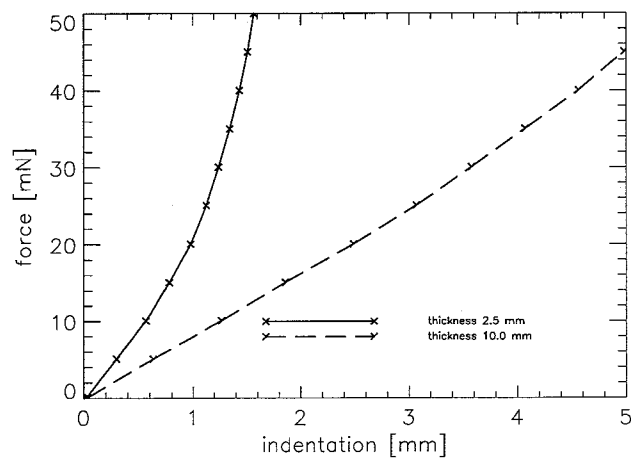


Figure 4.9: Results of quasistatic indentation test on Silgel 612, 2.5 and 10.0 mm thick

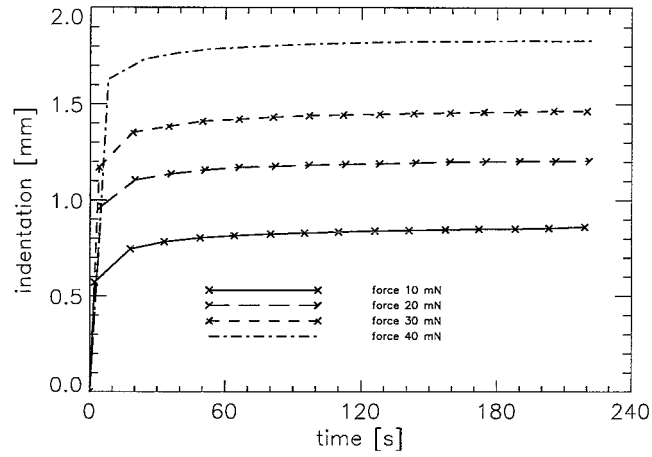


Figure 4.10: Results of creep indentation test on Silgel 612, 2.5 mm thick

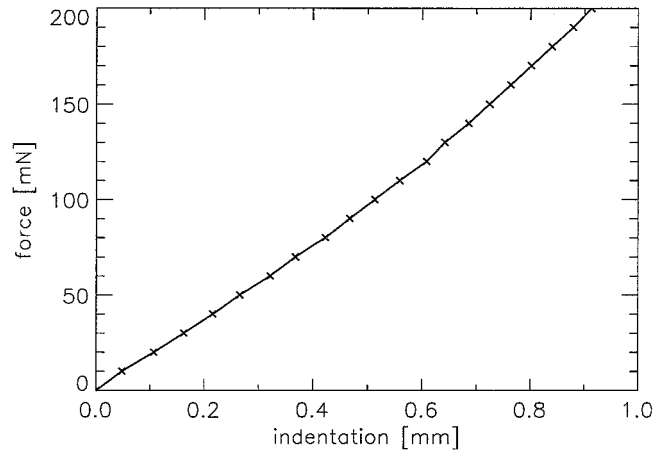


Figure 4.11: Results of quasistatic indentation test on artificial skin, with S612 2.5 mm and S601 0.82 mm thick

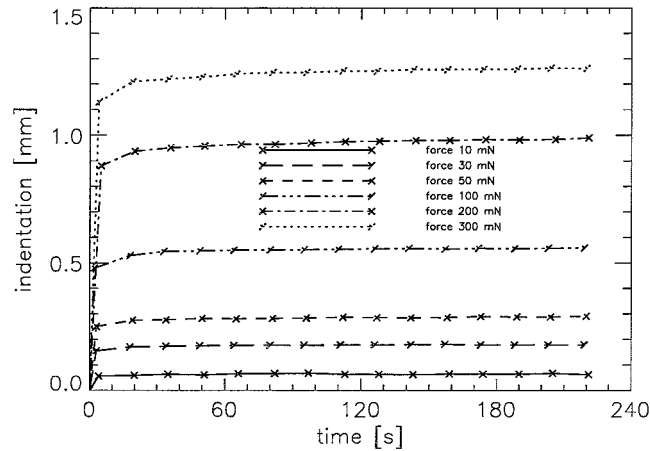


Figure 4.12: Results of creep indentation test on artificial skin, with S612 2.5 mm and S601 0.82 mm thick

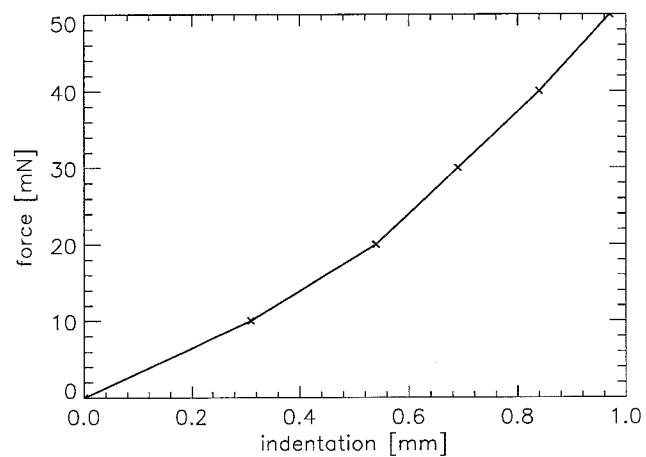


Figure 4.13: Results of an indentation test on human skin (shin), with the stratum corneum 0.010 mm thick, the dermis 1.2 mm and the subcutaneous fat layer 0.6 mm

Indentation test on human skin

Data of a quasistatic indentation test performed on the skin of a female was available. The indentation force was heightened in five steps to 50 mN . At the same shin site the skin and fat layer thickness were measured by means of the Cotech Dermal Depth Detector [Star 92], which measures layer thicknesses using the pulsed ultrasound technique. The thickness of the skin was 1.2 mm and the subcutaneous fat layer 0.6 mm .

Chapter 5

Numerical results

Tensile tests were performed on the Silgel materials as described in Chapter 4. With this data, parameters for the elastic and viscoelastic model are estimated. For the human skin layers also elastic and viscoelastic parameters are estimated from experimental data. This data is obtained from literature as described in Section 2.2. The estimation tool and all the estimations are described in Section 5.1.

With the determined parameters indentation tests are simulated for the artificial skin, its separate layers and for a human shin. The simulations are described, compared with the measurements and discussed in Section 5.2.

5.1 Parameter estimation

The parameter estimation tool Parfit, is described shortly in section 5.1.1. In Section 5.1.2 the parameters for the elastic material model are estimated from the various tensile experiments on the Silgel materials and skin layers. The same is done for the parameters of the viscoelastic model as far as relevant in Section 5.1.3.

5.1.1 Parameter estimation tool

At Philips Research Parfit, a parameter estimation tool was developed by [Star 94]. The Parfit version that is applied here uses the minimum variance estimator as described in Section 3.2. To run Parfit four input files are necessary; an `experiment.def` file, an `experiment.dat` file, an `experiment.sh` file and an `experiment.exe` file. In the file `experiment.def` the estimation problem is defined. This file contains information about which parameters have to be estimated, their initial conditions, the size of the covariances and the measurement data. The `experiment.dat` file involves information about the specific model and geometrical parameters. The `experiment.sh` file runs the executable file `experiment.exe`. The `experiment.exe` solves the problem analytically or writes the MARC input files, that are supplied to the MARC program.

The parameter estimations were performed with the results of the tensile tests. Therefore the analytical equations of a viscoelastic tie rod as derived in Chapter 3 were implemented in the c-source file `trek_vm.c` (see Appendix B) from which the executable `trek_vm.exe` was obtained.

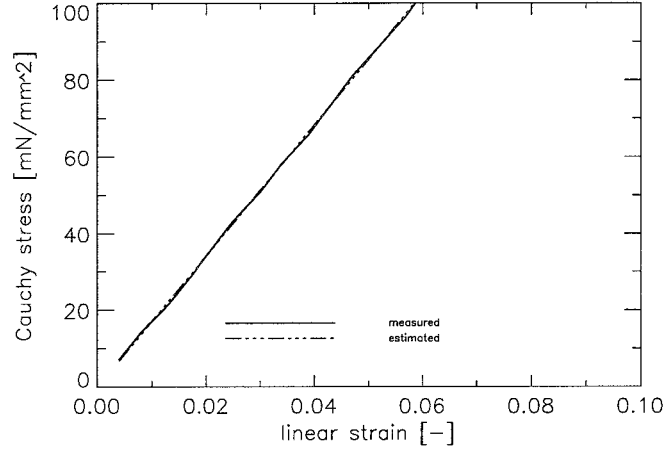


Figure 5.1: Results of parameter estimation tensile test on Silgel 601

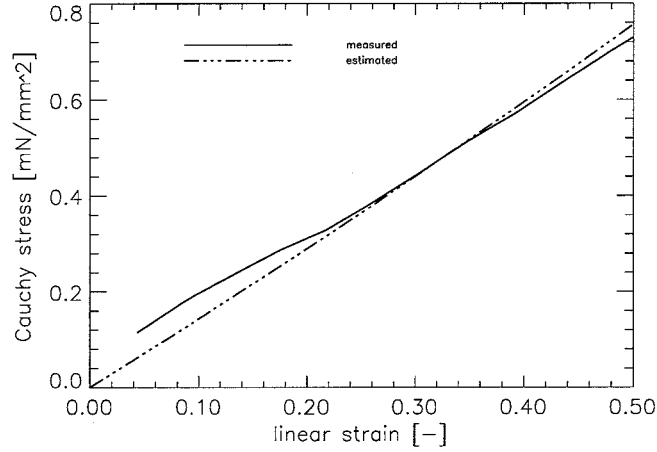


Figure 5.2: Results of parameter estimation from the tensile test on Silgel 612

5.1.2 Estimation with elastic model

For the estimation of the parameters of the elastic model, the data obtained from the quasistatic tensile tests was used. In all the estimations the observation error covariance was chosen

$\mathbf{R}_{k+1} = R \cdot \mathbf{I}$ with R the observation error multiplier and \mathbf{I} the identity matrix with size m equal to the number of measurements.

For the estimation of the parameters of Silgel 601 it was started with only one parameter, the Mooney-Rivlin parameter C_{10} . For the The observation error covariance multiplier R was chosen to equal 1.0 mN^2 and $\mathbf{Q}_k = 100 \text{ mN}^2/\text{mm}^4$. The final value for the first Mooney-Rivlin parameter was $C_{10} = 285 \text{ mN}/\text{mm}^2$ with standard deviation $1.1 \text{ mN}/\text{mm}^2$ ($\chi^2 = 3.5$, 15 observations). In Figure 5.1 the curve calculated with this estimated value and the measured curve are displayed. These curves are so close to each other that it is hard to distinguish them. The estimated value is very good and adding more Mooney-Rivlin parameters did not give further improvement.

To estimate the properties of Silgel 612 it was started with the first Mooney-Rivlin parameter C_{10} . The observation error covariance multiplier was $R = 1.0 \text{ mN}^2$ for every observa-

tion and $\underline{Q}_k = 100 \text{ mN}^2/\text{mm}^4$. The final estimation was $C_{10} = 0.239 \text{ mN}/\text{mm}^2$ standard deviation $0.0067 \text{ mN}/\text{mm}^2$ ($\chi^2 = 8, 12$ observations). The curve calculated with the estimated value of C_{10} and the measured curve are displayed in Figure 5.2. The calculated curve is quite close to the measured curve. This result could hardly be improved by using more Mooney-Rivlin parameters.

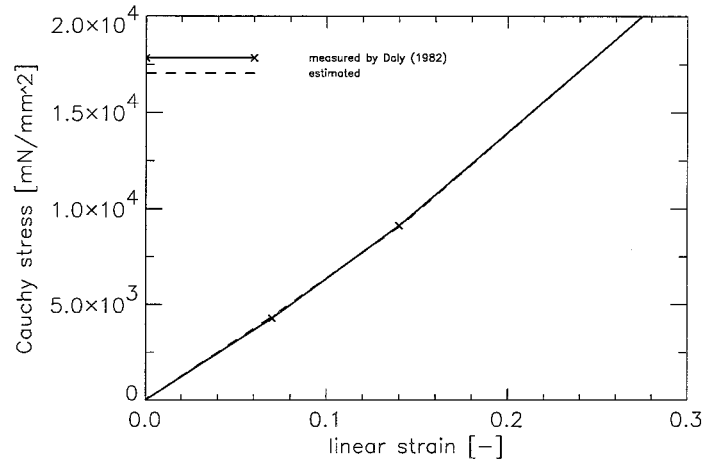


Figure 5.3: Results of an estimation from a tensile test on stratum corneum

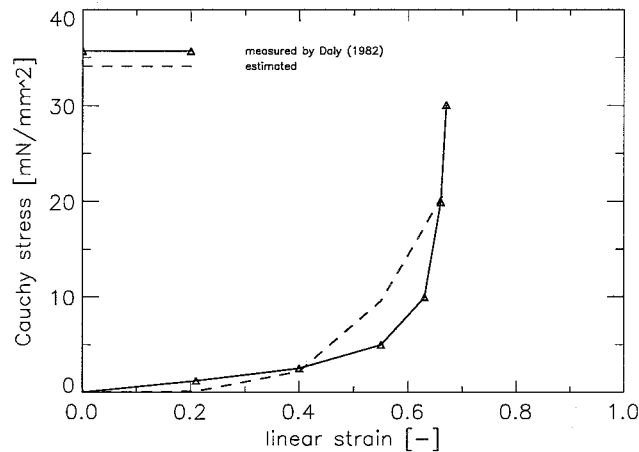


Figure 5.4: Results of an estimation from a tensile test on dermis

Elastic skin parameters

Similar to the way the elastic parameters of the S601 and the S612 were estimated, the parameters of the expanded Mooney-Rivlin model are estimated for the stratum corneum and the dermis.

[Wild 71] measured tensile characteristics of stratum corneum at different relative humidities. By linear interpolation a curve is found for 54 % RH as described in Section 2.2. From this curve the parameters for the expanded Mooney-Rivlin model were estimated with $R = 100 \text{ mN}^2$ and $\underline{Q}_k = 100 \text{ mN}^2/\text{mm}^4$ for each parameter. The final estima-

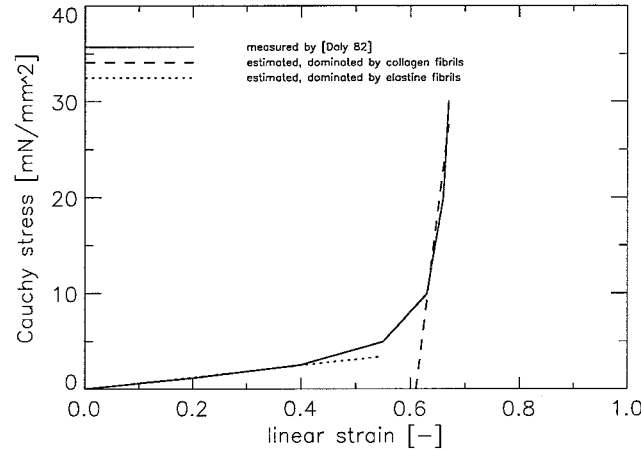


Figure 5.5: Results of estimating a tensile characteristic of dermis split up in a soft and a stiff part

tion of the parameters were $C_{10} = 205 \text{ mN/mm}^2$ with standard deviation 10 mN/mm^2 and $C_{30} = 103 \text{ mN/mm}^2$ with standard deviation 23 mN/mm^2 ($\chi^2 = 0.03$, 3 observations). It can be seen in Figure 5.3 that these parameters give a curve that is very close to the measured curve.

The parameters of the dermis were estimated with results of measurements performed by [Daly 82]. The error covariance multiplier R was taken equal to 1.0 mN^2 and the $\underline{Q}_k = 100 \text{ mN}^2/\text{mm}^4$ for each parameter. The estimated parameters of the expanded Mooney-Rivlin model were $C_{10} = -0.77 \text{ mN/mm}^2$ with standard deviation 0.5 mN/mm^2 and $C_{30} = 2.1 \text{ mN/mm}^2$ with standard deviation 0.2 mN/mm^2 ($\chi^2 = 44$, 6 observations). The negative parameter C_{10} gave the best results, but is physically not interpretable. The results of this estimation was not very satisfying, but could not be improved by adding more parameters.

As appears from Figure 5.4 the expanded Mooney-Rivlin model is not able to describe such a complex material as the dermis adequately. As described in Chapter 2 the dermis characteristic is mainly determined by two kinds of fibrils; elastine and collagen fibrils. The expanded Mooney-Rivlin model is not able to describe the behaviour of both kinds of fibrils with one set of elastic parameters, but perhaps it can describe both fibril characteristics separately.

For the next estimation the dermis tensile curve was split up in three parts; a part in which the linear strain is between zero and 0.40, a part in which the strain is larger than 0.61 and a part in between. In the first part the elastine fibrils dominate the mechanical behaviour, in the second the collagen fibrils and in the third a mix of both fibrils. For the first two parts the Mooney-Rivlin parameters can be estimated easily. The third part is the bottle neck in modelling, because of the large change in slope, that is caused by the straightening collagen fibrils. This part is left out of consideration here.

For the elastine part the R was chosen to be 1.0 mN^2 and the $\underline{Q}_k = 100 \text{ mN}^2/\text{mm}^4$. As Figure 5.5 shows a good performance could be obtained for the elastine part with parameter $C_{10} = 1.0 \text{ mN/mm}^2$ with standard deviation 0.5 ($\chi^2 = 0.03$, because of the linearity of the curve only 2 observations were taken). For the estimation of the part of the tensile characteristic of the dermis in which the collagen fibrils dominate, a strain shift of 0.61 was applied. Furthermore the R was taken equal to 1.0 mN^2 and the $\underline{Q}_k = 100 \text{ mN}^2/\text{mm}^4$.

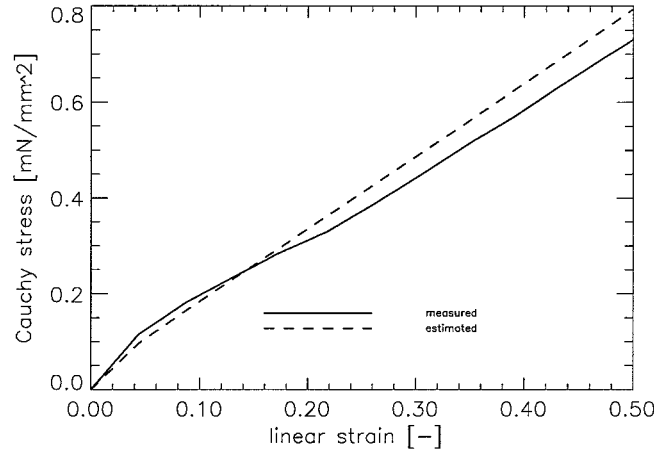


Figure 5.6: Results of the estimation of the quasistatic measurement on Silgel 612

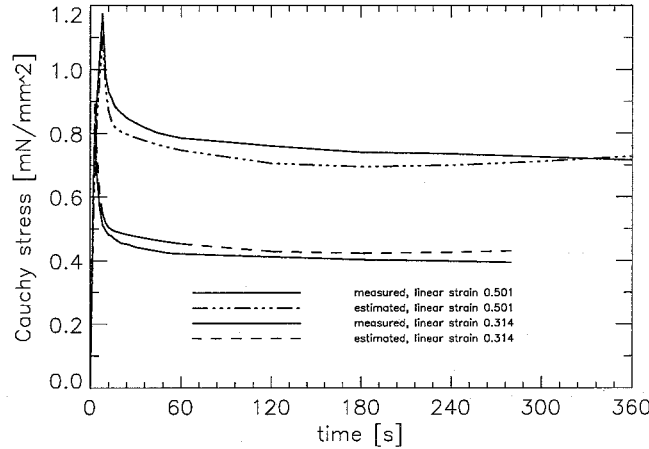


Figure 5.7: Results of the estimation of the relaxation experiments on Silgel 612

As it can be seen from Figure 5.5 the fit with $C_{10} = 49 \text{ mN/mm}^2$ and standard deviation 2 mN/mm^2 is close to the measured one ($\chi^2 = 6$, 3 observations).

5.1.3 Estimation with viscoelastic model

Silgel 601 does not show any identifiable time dependent behaviour in the indentation tests and tensile tests as described in Chapter 4. So adding a viscous part to its current elastic model is not necessary.

Silgel 612 on the contrary shows time dependent behaviour in the performed relaxation and creep experiments as described in the preceding. So it is probably useful to model it viscoelastic. Three experiments were used estimating the viscoelastic parameters; a quasistatic tensile test and two relaxation tensile tests. It was started with one relaxation time and one energy function multiplier. As initial value for the Mooney-Rivlin parameter C_{10} the value of the elastic estimation was chosen. The observation error covariance multiplier R was taken 1.0 mN^2 for all observations and the \underline{Q}_k was taken $100.0 \text{ mN}^2/\text{mm}^4$, 100.0 s^2 or 100 for the parameters. The performance could be improved by adding two more relaxation times and

energy function multipliers ($\chi^2 = 52.9$, total number of observations = 53) which furnished an acceptable curve for the quasistatic and the relaxation tensile experiments as can be seen in Figure 5.6 and Figure 5.7. The Cauchy stress of the relaxation curve with 0.50 strain tends to become larger after 300 seconds, which is physically not interpretable. This is caused by the measurement times of the relaxation curves that are not equal. As the relaxation curve with a strain of 0.31 ends, the estimation tends more towards the relaxation curve with strain 0.50.

The final estimations for the parameters and their standard deviations are displayed in Table 5.1.

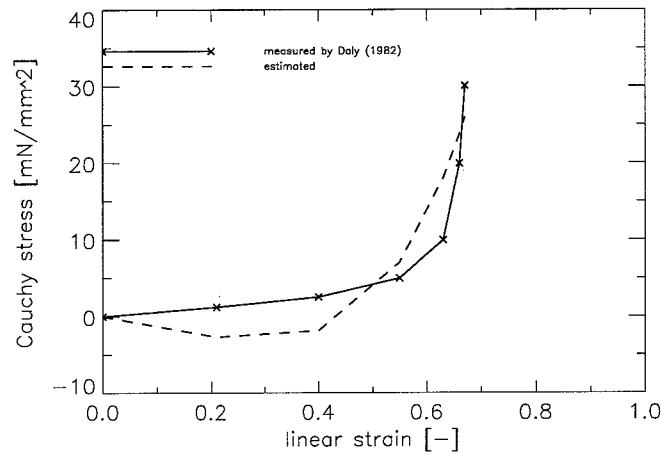


Figure 5.8: Results of the estimation of the tensile test on dermis

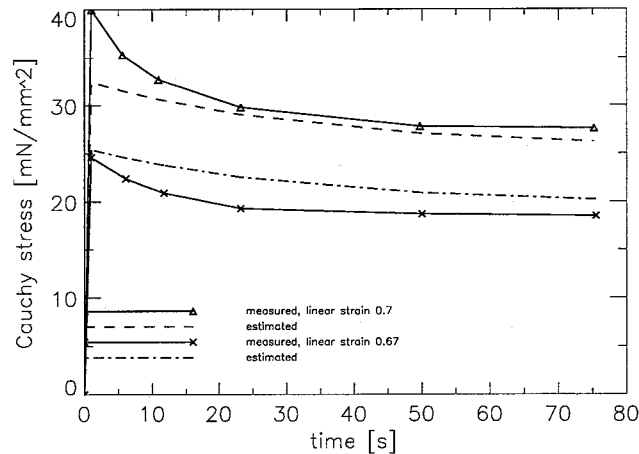


Figure 5.9: Results of estimation of the relaxation tensile tests on dermis

viscoelastic skin parameters

As described in the preceding in dry skin the stratum corneum is assumed to be elastic compared to the dermis. Only the dermis is considered to behave time dependent and so it is modelled viscoelastic.

To obtain viscoelastic parameters for the dermis a quasistatic and two relaxation tensile tests, performed by [Daly 82], were used. The observation error covariance multiplier was chosen to be $R = 1.0 \text{ mN}^2$ and the $Q_k = 100 \text{ mN}^2/\text{mm}^4, 100 \text{ s}^2$ or 100. The estimated parameters were $C_{10} = -2.9 \text{ mN}/\text{mm}^2$ with standard deviation $0.7 \text{ mN}/\text{mm}^2$ and $C_{30} = 2.4 \text{ mN}/\text{mm}^2$ with standard deviation $0.4 \text{ mN}/\text{mm}^2$ ($\chi^2 = 97$, total number of observations = 18). The estimation results are not very satisfying (see Figure 5.8 and 5.9). The stress even becomes below zero, which is physically not interpretable. Evidently it is not possible to describe such a complex fibre reinforced material as dermis with one set of viscoelastic parameters. But perhaps it is possible to improve the estimation result by splitting the tensile characteristic up.

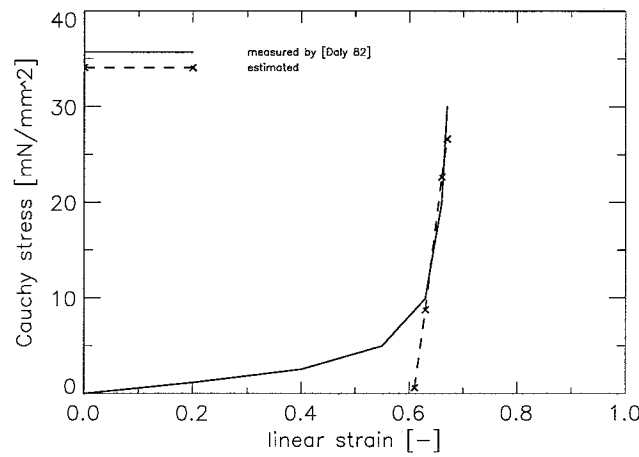


Figure 5.10: Results of the estimation of the tensile test on dermis

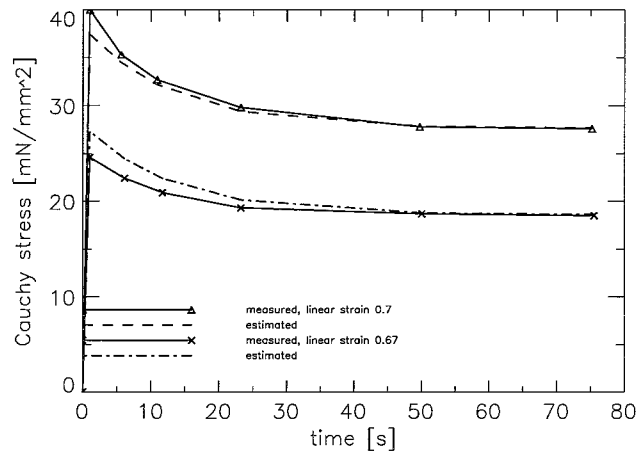


Figure 5.11: Results of the estimation of the relaxation tensile tests on dermis

In the same way as with the estimation of the elastic dermis parameters, the tensile curve was split up for the estimation of viscoelastic parameters. At low linear strains (< 0.4) the dermis can be considered elastic, because the tensile properties are dominated by elastine fibrils. At larger strains the dermis can be considered viscoelastic, because of the interaction of viscoelastic collagen fibrils. The relaxation curves used for estimating the viscoelastic

	C_{10} [$\frac{mN}{mm^2}$]	C_{30} [$\frac{mN}{mm^2}$]	γ_1 [—]	ν_1 [s]	γ_2 [—]	ν_2 [s]	γ_3 [—]	ν_3 [s]
<i>Artificial skin</i>								
Silgel 601	285(1.1)							
Silgel 612	0.24(0.01)							
Silgel 612, vis.	0.63(0.04)		0.58(0.03)	2.5(0.2)	0.12(0.1)	88(72)	-0.7(1)	3 10 ⁴ (1 10 ²)
<i>Human skin</i>								
Str. corneum	205(10)	103(23)						
Dermis	-0.77(0.5)	2.1(0.2)						
Dermis, vis.	-2.9(0.7)	3.4(0.4)	0.37(0.06)	33(15)				
Elastine part	1.0(0.5)							
Collagen part	49(2)							
Coll. part, vis.	62(6)		0.47(0.05)	13(3)				

Table 5.1: Elastic and viscoelastic (vis.) parameters of artificial skin and human skin (standard deviations between brackets)

parameters of dermis are related to large strains (0.67 and 0.70). So only the part of the dermis tensile characteristic where collagen fibrils are involved has to be taken into account.

Estimating the viscoelastic parameters of the dermis with the adapted tensile curve a strain shift of 0.61 was applied. The R was taken equal to 1.0 mN^2 and Q_k equal to 100 mN^2/mm^4 , 100 s^2 or 100 for the parameters. The final estimations of the viscoelastic parameters are gathered in Table 5.1 ($\chi^2 = 15$, total number of observations = 15). Only one relaxation time is found, which is unusual for such a complex material as dermis. Perhaps other relaxation times are too short to measure with the measuring equipment [Daly 82] used. The curves calculated with these parameters are acceptable close to the measured curves (see Figure 5.10 and Figure 5.11).

All the estimated parameters of the artificial skin layers and the human skin layers are gathered in Table 5.1.

5.2 Experiment simulation

In this section simulations of indentation experiments are compared with the measured indentation curves as described before in Chapter 4. In Section 5.2.1 the simulation set-up is described shortly and in Section 5.2.2 the simulation results.

5.2.1 Simulation set-up

A finite element model was constructed with the finite element package MARC. The skin in this model consists of three layers; the stratum corneum (or S601), the epidermis without

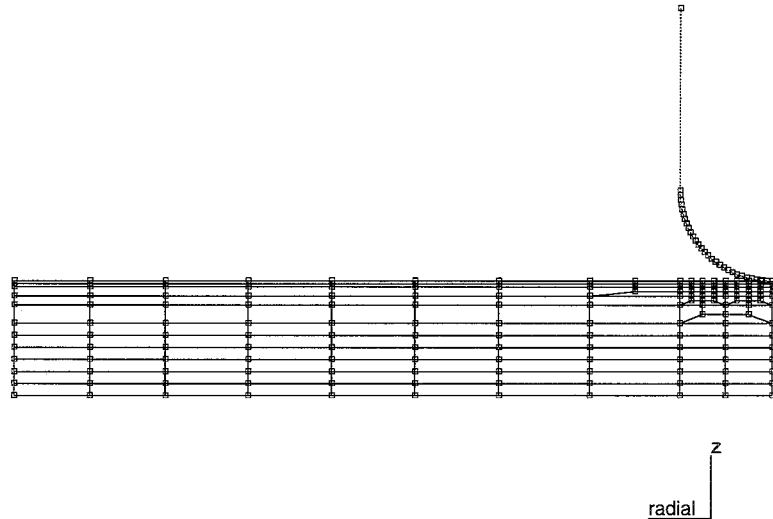


Figure 5.12: Mesh for the indentation simulation

stratum corneum and the dermis (or S612) and the subcutaneous fat tissue. In a two layer model the last two layers have the same material properties and in a one layer model all the layers have the same material properties. All the layers were modelled with element number 119, which is an incompressible quadrilateral axisymmetric element. It uses linear interpolation for the displacements and the pressure is constant over the element.

The skin was touched by the indenter, which was modelled as a rigid body. The mesh is shown in Figure 5.12. On the indenter a force was applied with the same load steps and time steps as in the experiments. The number of increments per time step varied from 50 increments with the Silgel 612 to 10 with the Silgel 601 and 5 with the artificial and human skin.

5.2.2 Simulation results

The indentation test on a 10 mm thick S601 layer was simulated with the elastic parameters estimated from the tensile test. In Figure 5.13 the measured and simulated curves are displayed. The curves are close to each other, although there is a systematic error visible.

The indentation experiment on S612 was simulated with both the elastic and the viscoelastic parameters estimated from the tensile tests. The elastic simulation caused some problems at forces larger than 20 mN. The indentation depth at these forces is too large. The elements go partly through the probe. As it can be seen in Figure 5.14 the measured curve is much stiffer than the elastic simulation. The viscoelastic curve on the contrary is close to the measured curve.

In Figure 5.15 the elastic simulation, the viscoelastic simulation and the quasistatic measurement of the artificial skin are displayed. In the elastic simulation the elastic parameters, determined from the tensile tests, are used for both the S612 and S601. In the viscoelastic

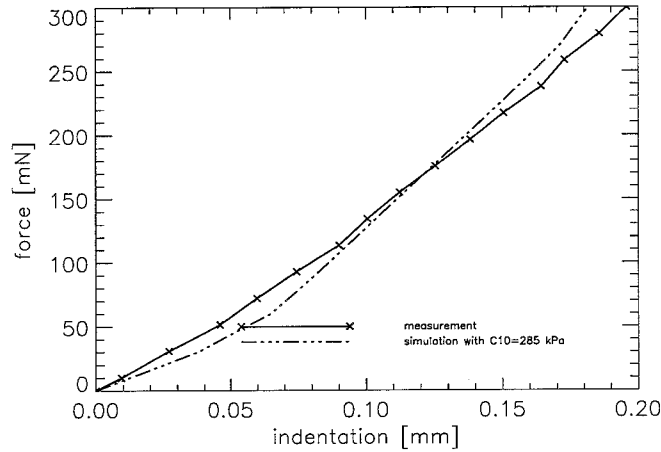


Figure 5.13: Simulation of the indentation test on Silgel 601

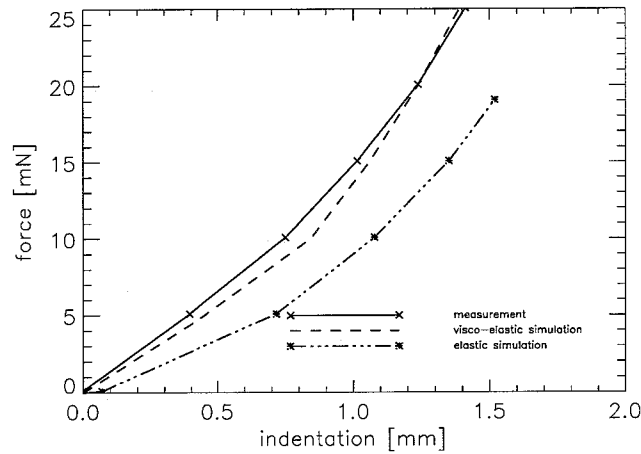


Figure 5.14: Simulation of the indentation test on Silgel 612

simulation the viscoelastic parameters for the S612 and the elastic parameters for the S601 are taken. For the artificial skin the simulation with elastic parameters is in general a little better than the simulation with the viscoelastic parameters, but both simulations are too stiff at large forces. At low forces ($< 20 \text{ mN}$) the measured curve is close to the viscoelastic simulation. The worse performance at large force could be explained by slipping of the top layer due indentation forces.

Creep indentation experiments on artificial skin were simulated with viscoelastic parameters. The simulated creep curves are a little too stiff at large forces (see Figure 5.16 at 100 and 300 mN), like the viscoelastic quasistatic curve in Figure 5.15. Besides positioning errors could have caused deviations.

Simulation with human skin

The quasistatic indentation test performed on human shin as described before in Section 4.2, was simulated. By lack of knowledge of the mechanical properties of the subcutaneous fat layer, it is assumed that this layer has the same properties as the dermis. However it is

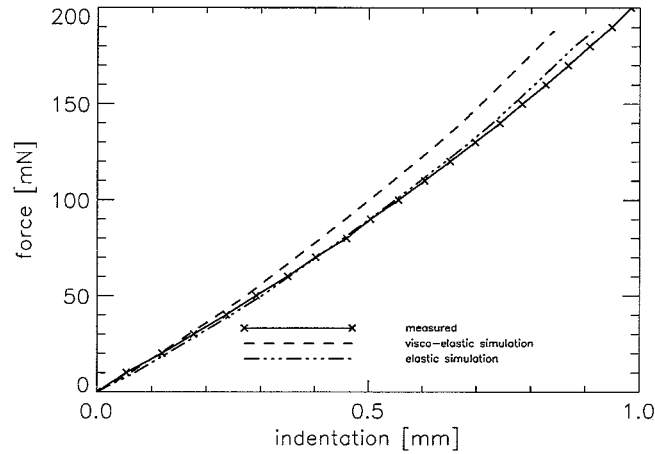


Figure 5.15: Simulation of the indentation test on artificial skin

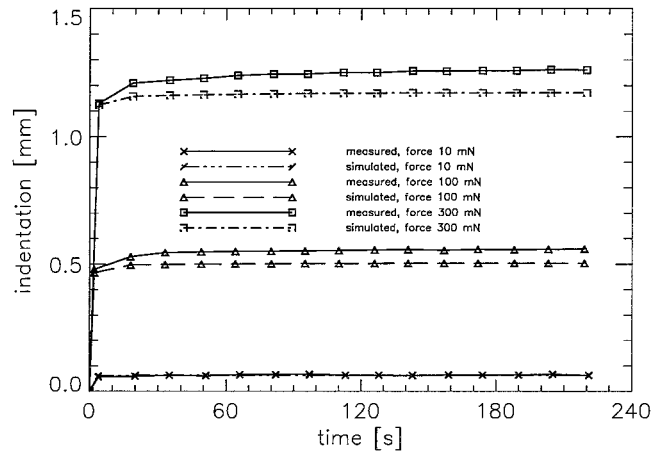


Figure 5.16: Simulation of the creep indentation tests on artificial skin with viscoelastic parameters

expected that the dermis is stiffer than the subcutaneous fat layer, because the fat layer does not have a proper structure and it does not contain reinforcing fibrils, like the dermis. The shin bone is directly below the fat layer, which is supposed to be rigid.

It was expected that the collagen fibrils were not stretched in the dermis, when an indentation force of at most 50 *mN* was applied. So at first the dermis was given low-strain elastic parameters.

It was supposed that the dermis' fibrils are situated in the plane parallel to the surface, neglecting the influence of deformation due indentation. So the strains of interest are the radial and tangential strain. These two strains are equal. The size of the radial strain in the skin is shown in Figure 5.17, at a force of 50 *mN*. Only in a small area just under the probe elastic strains larger than 0.4 were observed. This indeed means that mainly elastine fibrils are involved. In the simulation the skin goes partly through the probe (see Figure 5.17). The influence of this defect is very limited as long only one node is 'inside' the probe.

For the properties of the stratum corneum the relative humidity of the environment is important [ParkII 72]. This was not measured during the experiment, so a quite normal

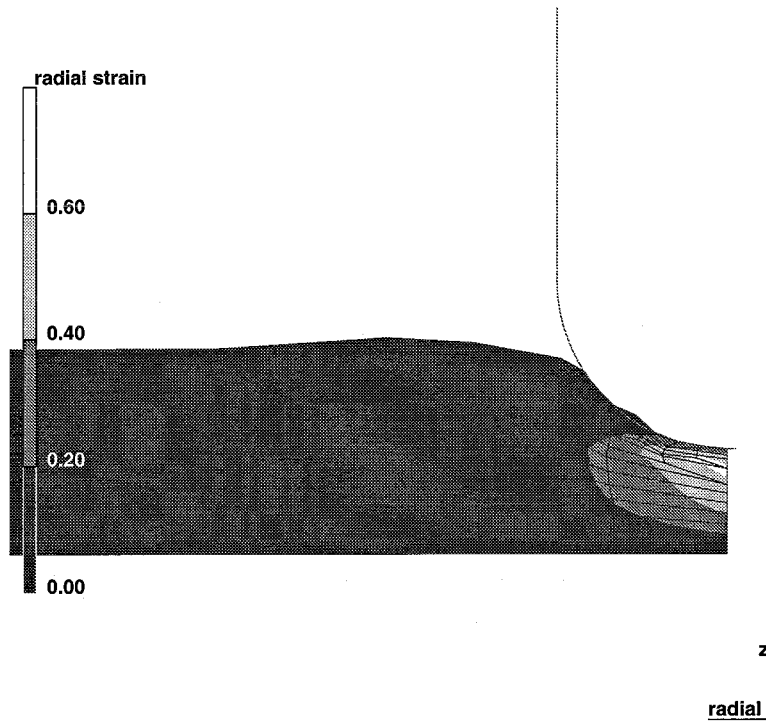


Figure 5.17: Elastic strains in a simulation of an indentation test on human skin when the indentation force is 50 mN applied

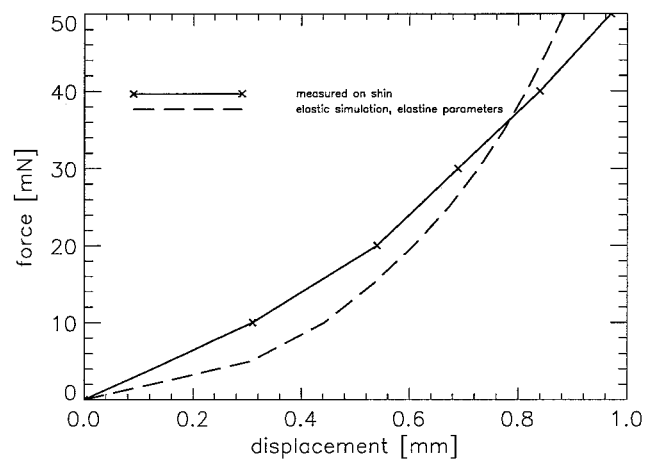


Figure 5.18: Simulation of the quasistatic indentation test on in vivo skin of the shin

relative humidity of 54 % was assumed.

In Figure 5.18 the indentation curve on the human shin is displayed and the curve of the simulation with the elastic parameters for the stratum corneum and for the dermis the low-strain elastic parameters.

Although the simulated curve and the measured curve are quite close, some considerations have to be made. The first is that in the simulation model the subcutaneous fat layer is assumed to have the same properties as the dermis. As mentioned before it is plausible that the fat layer is softer. So modelling the fat layer properly would force the simulated curve to become softer. An other assumption made in the simulation is that the skin is not pre-strained. In vivo skin has a pre-strain [Jong 95]. This would results in a stiffer indentation curve, because the elastine fibrils are stretched already and even the collagen fibrils could play a part in this. These two assumptions have a contrary effect on the indentation characteristic. So it is not possible to give a statement about how the indentation curve would change if the model would be proper.

Perhaps it is not the fibrous structure of the dermis that dominates the indentation behaviour of the dermis, but the properties of the matrix of ground substance, which may also be viscoelastic. If that is true, the parameters of dermis estimated from a tensile test cannot be used for the simulation of an indentation test, because the tensile behaviour is mainly determined by the fibrous structure of dermis.

Chapter 6

An application

To determine whether viscoelastic modelling of skin is required in shaving simulations, a simulation of a Lady-shave moving along skin was performed. The parameters used for this simulation were obtained from the estimations of tensile tests on dermis and stratum corneum as described in Section 5.1. In Section 6.1 the simulation set-up is described and in Section 6.2 the results of the simulations are presented.

6.1 Simulation set-up

Within Philips Research a finite element model of a Lady-shave moving along the skin was available (see Figure 6.1). Layer thicknesses were obtained from skin of the shin site of a female as used before in the simulation of the indentation test on skin (see Section 5.2). The same assumptions involving the subcutaneous fat layer and prestrain were made here. The

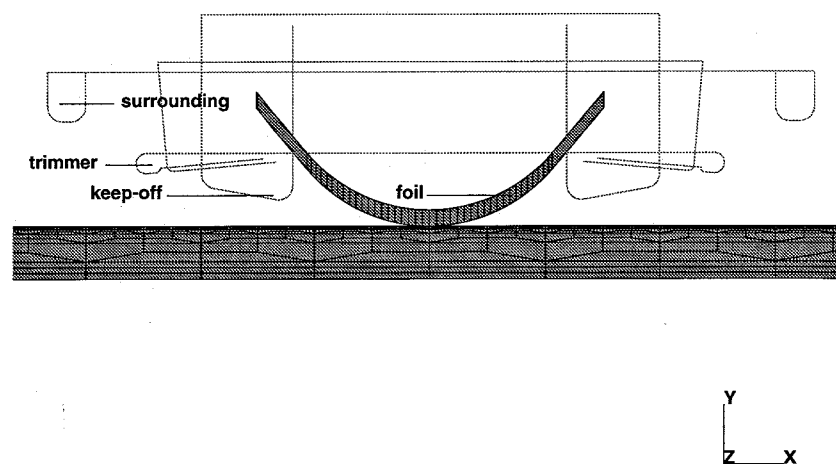


Figure 6.1: Mesh for the simulation of a Lady-shave moving along the shin of a female

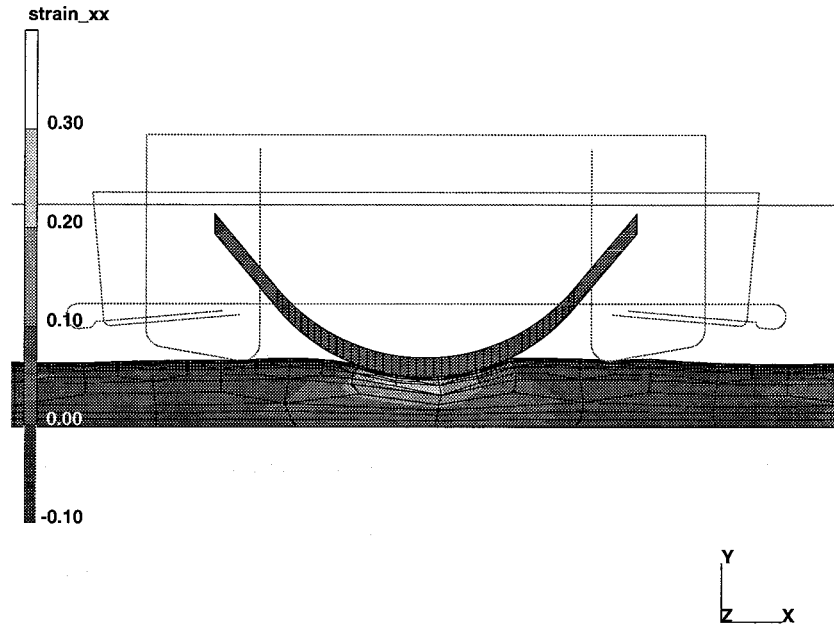


Figure 6.2: Simulation of a Lady-shave moving along elastic modelled skin, with the linear strain in x direction

shaver head parts, all modelled as rigid bodies, consist of a shaving foil, two skin keep-offs (or ornamental strips), two trimmers and the surrounding. The shaving foil is assumed to be spring-loaded by a spring with a stiffness of 1.0 N/mm and a preload of 0.5 N . The shaving foil is modelled 'blind', without any openings. It is assumed that no friction occurs between skin and Lady-shave. The force by which the Lady-shave is applied to the skin is taken equal to 1 N .

6.2 Simulation results

At first it is supposed that the strains are not very large in the dermis and so mainly elastine fibrils are involved. The dermis was initially given low strain elastic parameters as determined in Section 5.1. The indentation force of 1 N is applied in 0.02 seconds. As shaving velocity 10 cm/s was taken, which is an experimentally determined average value. This velocity is established by moving the lower edge of the skin to the right.

The elastic deformation should be symmetrically, but as it can be seen in Figure 6.2 at the right hand side the skin sticks more to the shaving foil than on the left hand side. This is probably caused by the contact algorithm, that has problems releasing the skin.

Neglecting the influence of deformations, it is supposed that the dermis' fibrils are situated in the xz plane. So the strains of interest are the strains in x - and z -direction. The strain in z direction is very low (± 0). It can be seen in Figure 6.2 that the strain in x -direction is smaller than 0.30 . So it is not expected that collagen fibrils are stretched.

According to this the skin could be modelled elastic in shaving simulations. However when skin is shaved viscous effects are observed. To become an idea of how skin with viscoelastic properties react to a moving shaving system, the simulation is repeated with for the dermis

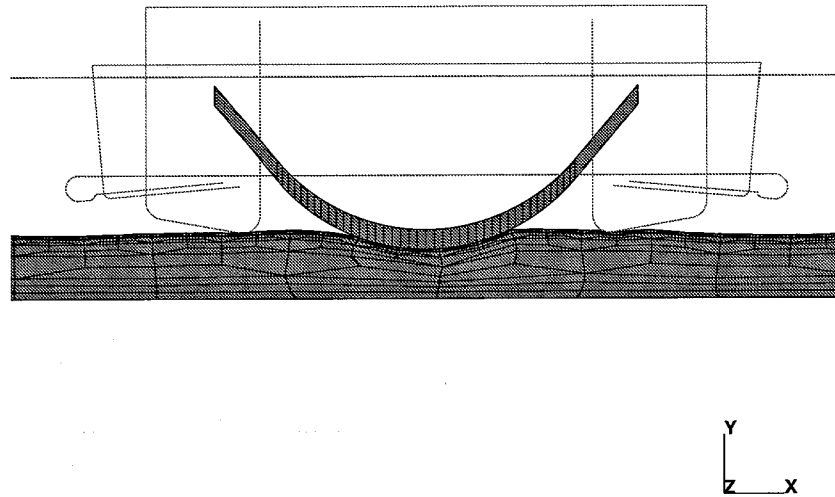


Figure 6.3: Simulation of a Lady-shave moving along viscoelastic modelled skin

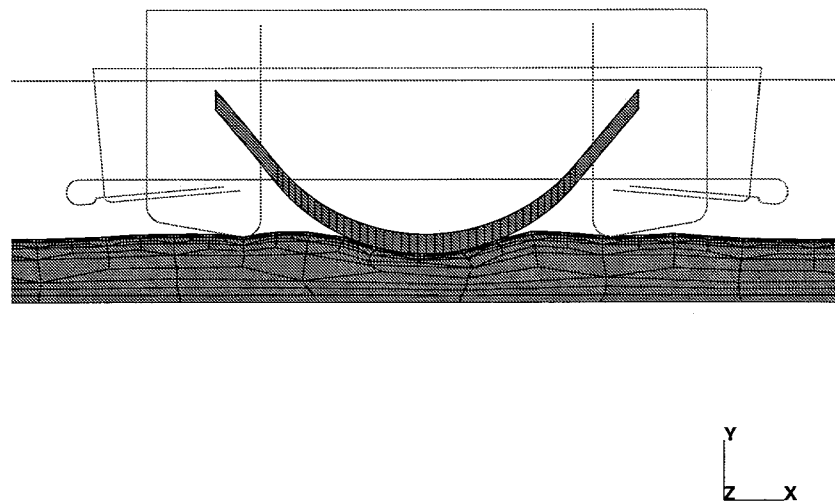


Figure 6.4: Simulation of a Lady-shave moving slow along viscoelastic modelled skin

low strain (elastine) elastic Mooney-Rivlin parameters and the relaxation time and energy function multiplier of the high strain (collagen) part. Results of this simulation are restored in Figure 6.3. From this figure no apparent difference with the elastic simulation of Figure 6.2 can be distinguished. This can be explained by the fact that the relaxation time used is much larger than the characteristic shaving process time and so it does not have any effect.

A measure for the characteristic process time can be calculated with the characteristic apparatus size divided by the shaving velocity. For the current shaving process the characteristic apparatus size is about 1 *cm* (the width of the foil) and the velocity 10 *cm/s*. So the characteristic process time is about 0.1 s. This characteristic process time is about 100 times shorter than the relaxation time, so $\nu/t_p \gg 1$ and the material behaves almost elastic as described in Section 3.1.3.

So the found relaxation time of dermis only has a recognizable influence when it is focussed on longer process times. So when the moving velocity of the Lady-shave is reduced to 0.01 *cm/s* and the indentation force of 1 *N* is applied in 20 seconds, the viscoelastic effect should be recognizable. The result of this simulation is shown in Figure 6.4. This indentation is asymmetrical. The skin on the left hand side is a little higher than on the right hand side and the left keep-off pushes further in the skin than the right one.

So as appears from this the relaxation time for the dermis found in the preceding is only interesting at slow shave movements. In normal shaving processes it does not play a role. For those it must be focussed on shorter relaxation times. Short relaxation times cannot be determined with the experiments used. Therefore dynamic measuring is useful. The experimental-numerical approach that is used in this report can still be useful. The tensile test can be performed with a sinusoidal extension. The indentation test can be performed with a sinusoidal indentation added to a static indentation. Varying the frequency of the excitations gives the opportunity to become information at different time scales.

Chapter 7

Conclusions and recommendations

7.1 Conclusions

Parameter estimations

From tensile tests (visco-)elastic parameters were estimated for the separate layers of the artificial skin and for the dermis and stratum corneum of human skin.

For both layers of the artificial skin adequate (visco-)elastic parameters were estimated.

For the stratum corneum elastic parameters were estimated. Estimating the (visco-)elastic parameters for the dermis was hard. To obtain an acceptable estimation the dermis tensile characteristic was according to its structure split up into three parts; a part for low strains, where mainly elastine fibrils are involved, a large strain part, where mainly collagen fibrils are involved and a part in between. For the part with low strain and large strain adequate parameters were estimated.

It appears from this that when there are large variations in strains the behaviour of the dermis cannot be described with the simple phenomenological Mooney-Rivlin model. It may be advantageous to use a structural model that takes the fibrous structure of dermis into account, like the Lanir model [Voord 96].

Indentation test simulation

To verify the estimated parameters indentation tests were simulated and performed on the artificial skin and its separate layers. Besides results of an indentation test on human skin was available.

Simulations of the indentation tests on the rubbers performed with elastic and viscoelastic parameters, obtained from tensile tests, gave reasonable results. In case of S612 the viscoelastic simulation was better than the elastic. In case of the artificial skin the elastic simulation fits best, but both simulations were too stiff. This could be caused by slipping of the top layer.

Simulation of the indentation test on human skin was quite good using low strain elastic parameters. Although a few rough assumptions were made, concerning pre-strain and the properties of the subcutaneous fat layer.

Shaving simulation

A simulation of a Lady-shave moving along human skin is performed.

The relaxation time of dermis estimated from tensile tests is not interesting for the simulated shaving process, because it is too large compared to the characteristic process time.

Short relaxation times of skin (order 0.1 seconds) are interesting for shaving processes. It is not possible to determine these from the experiments used.

7.2 Recommendations

When large changes in strain in the dermis have to be described, the phenomenological Mooney-Rivlin model is not sufficient. A structure related model may be advantageous. Such a structural model should at least model the stratum corneum and the fibrous structure of the dermis and perhaps the ground substance of the dermis. The dermis should be modelled viscoelastic. This viscoelastic behaviour can be ascribed to the collagen fibrils and perhaps also to the ground substance.

Although quite some knowledge is available about skin and shaving processes, research is needed to investigate the various parts of a structural skin model for shaving applications. Therefore the following can be considered.

- When skin is shaved it is indented and at the same time it is stretched. The tensile behaviour of skin is mainly determined by the stratum corneum and the fibrous structure of dermis. Indenting in vivo skin, the behaviour is determined by the stratum corneum, the dermis, the hypodermis and the underlying tissue, for example muscles. About the indentation characteristics of the various layers is not much known. It is possible that not the fibrous structure of dermis, but the ground substance dominates the indentation behaviour, because the fibrous structure is situated in the plane parallel to the skin surface which is mostly perpendicular to the indentation direction. Focusing on in vitro experiments this can for example be investigated by applying indentation tests and tensile tests to dermis. From the tensile test by which the fibrous structure of dermis dominates the behaviour, parameters can be estimated. If it is possible to describe the indentation tests with these parameters, the indentation behaviour of dermis is also dominated by the fibrous structure. If not, probably the ground substance dominates indentation behaviour.
- Focusing on in vivo experimenting it is useful to gain more information from an indentation test for example by measuring the various layer thicknesses during indenting. This is possible with ultrasound measuring for example with the Dermalcan.
- Short relaxation times of skin (order 0.1 seconds) are interesting for (Lady-)shaving processes. It is not possible to determine such a short relaxation times from the experiments used in this project. To determine these, dynamic measuring could be useful. The experimental-numerical approach used in this report can be carried out with sinusoidal excitations with varying frequencies in the tensile tests and in the indentation tests. It could be started analysing dynamic indentation tests with the EDM [Bosm 88].
- For the verification of shaving simulations more knowledge is needed about skin deformations that occur during the interaction with apparatus. To measure strains at the skin surface the marker technique used by [Voord 96] can be adapted for larger strains.

Bibliography

- [Bosm 88] Bosman, H., Vos, R.,
The mechanical properties of human skin, Philips Nat.Lab. report No. 6266, Eindhoven, 1988
- [Chris 77] Christensen, M.S., Hargens III, C.W., Nacht, S., Gans, E.H.,
Viscoelastic properties of intact human skin: instrumentation, hydration effects and the contribution of the stratum corneum, Journal of investigative dermatology 69, pages 282-286, 1977
- [Daly 82] Daly, H.D.,
Biomechanical properties of dermis, The journal of investigative dermatology 79, pages 17-20, 1982
- [Druot 85] Druot, P., Rochefort, A., Oytana, C., Agache, P.,
In vitro stress relaxation tests of human stratum corneum, Bioengineering and the skin Vol. 1 No. 2, pages 141-156, 1985
- [Hool 80] Hooley, C.J., McCrum, N.G.,
The viscoelastic deformation of tendon, J. Biomechanics Vol. 13, pages 521-528, 1980
- [Jans 95] Jansen, M.Y.,
An artificial skin for shaving applications, a first investigation, Eindhoven university of technology WFW report No. 95.094, Eindhoven, 1995
- [Jong 95] Jong, L.A.M.,
Pre-tension and anisotropy in skin, modelling and experiments, Master of Science Thesis, Eindhoven university of technology WFW report No. 95.102, Eindhoven, 1995
- [North 78] North, J.F.,
The influence of strain rate on the mechanical properties of human skin and subcutaneous tissue, The south african mechanical engineer Vol. 28, pages 124-127, 1978
- [Marc 94] MARC Analysis Research Corporation
User information, volume A, C, California, 1994
- [Minns 73] Minns, R.J., Soden, P.D., Jackson, D.S.,

-
- The role of the fibrous components and ground substance in the mechanical properties of biological tissues: a preliminary investigation*, J.Biomechanics Vol. 6, pages 153-165, 1973
- [Oom 72] Oomens, C.W.J.,
Constitutieve modellen, diktaat vakgroep Fundamentele Werktuigbouwkunde, T.U. Eindhoven, 1992
- [ParkI 72] Park, A.C., Baddiel, C.B.,
Rheology of stratum corneum I: A molecular interpretation of the stress-strain curve, J. of the society of cosmetic chemists Vol. 23, pages 3-12, 1972
- [ParkII 72] Park, A.C., Baddiel, C.B.,
Rheology of stratum corneum II: A physico-chemical investigation of factors influencing the water content of the corneum, J. of the society of cosmetic chemists Vol. 23, pages 13-21, 1972
- [Rat 94] Ratingen, M.R.,
Mechanical Identification of inhomogeneous solids, A mixed numerical experimental approach, PhD Thesis, chap. 2, Eindhoven university of technology, Eindhoven, 1994
- [Sav 82] Savenije, E.P.W.,
Structure and mechanical properties of human hair and skin, Philips Nat.Lab. report No. 5806, Eindhoven, 1982
- [Schr 91] Schreurs, P.J.G.,
Continuümsmechanica, diktaat vakgroep Fundamentele Werktuigbouwkunde, T.U. Eindhoven, 1991
- [Simo 87] Simo, J.C.,
On a fully three-dimensional finite-strain viscoelastic damage model: formulation and computational aspects Computer methods in applied mechanics and engineering 60, pages 153-173, 1987
- [Star 94] Starmans, F.J.M.,
Parfit: a parameter estimation tool, Philips Nat.Lab. report No. 6712, Eindhoven, 1994
- [Star 92] Starmans, F.J.M.,
Skin thickness measurements with pulsed ultrasound, Philips Nat.Lab. Technical Note No. 347/92, Eindhoven, 1992
- [Voord 96] Voorden, W.K.L.,
Characterization of the in-plane mechanical behaviour of human skin, a mixed numerical-experimental approach employing a structural skin model, Master of Science Thesis, Eindhoven university of technology WFW report No. 96.073, Eindhoven, 1996

- [Vos 88] Vos, R.,
The mechanical properties of human skin, User guide for the electro-dynamometer, Philips Nat.Lab. report No. 078/88, Eindhoven, 1988
- [Wild 71] Wildnauer, R.H., Bothwell, J.W., Douglass, A.B.,
Stratum corneum biomechanical properties, I. Influence of relative humidity on normal and extracted human stratum corneum, The journal of investigative dermatology Vol. 56, No. 1, 1971

Appendix A

The Piola-Kirchoff stress

A.1 The elastic Piola-Kirchoff stress

From the Clausius-Duhem inequality the next equation for the Piola-Kirchoff stress could be determined (see Section 3.1).

$$\mathbf{S} = \rho_0 \frac{\partial \Psi}{\partial \mathbf{E}} \quad (\text{A.1})$$

The elastic strain energy function is defined in Equation A.2 (or 3.4):

$$\Psi = U^0(J) + \bar{\Psi}^0(\bar{\mathbf{E}}) \quad (\text{A.2})$$

Substituting Equation A.2 into Equation A.1 it follows for the Piola-Kirchoff stress that

$$\mathbf{S} = \rho_0 \frac{\partial U^0(J)}{\partial \mathbf{E}} + \rho_0 \frac{\partial \bar{\Psi}^0(\bar{\mathbf{E}})}{\partial \mathbf{E}} \quad (\text{A.3})$$

This can be written as:

$$\mathbf{S} = \rho_0 \frac{\partial U^0(J)}{\partial J} \frac{\partial J}{\partial \mathbf{C}} : \frac{\partial \mathbf{C}}{\partial \mathbf{E}} + \rho_0 \frac{\partial \bar{\Psi}^0(\bar{\mathbf{E}})}{\partial \bar{\mathbf{E}}} : \frac{\partial \bar{\mathbf{E}}}{\partial \mathbf{E}} \quad (\text{A.4})$$

With:

$$\frac{\partial J}{\partial \mathbf{C}} = \frac{1}{2} J \mathbf{C}^{-1} \quad (\text{A.5})$$

$$\frac{\partial \mathbf{C}}{\partial \mathbf{E}} = \frac{\partial (2\mathbf{E} + \mathbf{I})}{\partial \mathbf{E}} = 2^4 \mathbf{I} \quad (\text{A.6})$$

$$\frac{\partial \bar{\mathbf{E}}}{\partial \mathbf{E}} = \frac{\partial \frac{1}{2}(\bar{\mathbf{C}} - \mathbf{I})}{\partial \mathbf{E}} = \frac{\partial \frac{1}{2}(J^{-\frac{2}{3}} \mathbf{C} - \mathbf{I})}{\partial \mathbf{E}} = J^{-\frac{2}{3}} ({}^4\mathbf{I} - \frac{1}{3} \mathbf{C} \mathbf{C}^{-1}) \quad (\text{A.7})$$

in which $\bar{\mathbf{C}} = \bar{\mathbf{F}}^c \bar{\mathbf{F}}$. Substituting Equation A.5, A.6 and A.7 into Equation A.4 (or Equation 3.7) gives:

$$\mathbf{S} = \rho_0 J \frac{\partial U^0}{\partial J} \mathbf{C}^{-1} + \rho_0 J^{-\frac{2}{3}} \frac{\partial \bar{\Psi}^0}{\partial \bar{\mathbf{E}}} : ({}^4\mathbf{I} - \frac{1}{3} \mathbf{C} \mathbf{C}^{-1}) \quad (\text{A.8})$$

A.2 The viscoelastic Piola-Kirchoff stress

For the viscoelastic case two terms are added to the strain energy function of Equation A.2:

$$\Psi(\mathbf{E}, \mathbf{Q}) = U^0(J) + \bar{\Psi}^0(\bar{\mathbf{E}}) - \mathbf{Q} : \bar{\mathbf{E}} + \Psi_I(\mathbf{Q}) \quad (\text{A.9})$$

$\Delta\Psi$ is defined as:

$$\Delta\Psi(\mathbf{E}, \mathbf{Q}) = -\mathbf{Q} : \bar{\mathbf{E}} + \Psi_I(\mathbf{Q}) \quad (\text{A.10})$$

Calculating the Piola-Kirchoff stress $\Delta\mathbf{S}$ due the viscous term $\Delta\Psi$ the next equation is obtained.

$$\Delta\mathbf{S} = \rho_0 \frac{\partial \Delta\Psi}{\partial \mathbf{E}} = \rho_0 \frac{\partial(-\mathbf{Q} : \bar{\mathbf{E}})}{\partial \mathbf{E}} + \rho_0 \frac{\partial \Psi_I(\mathbf{Q})}{\partial \mathbf{E}} \quad (\text{A.11})$$

The last term is zero, because it is independent of the Green-Lagrange strain \mathbf{E} . So Equation A.11 becomes:

$$\Delta\mathbf{S} = -\rho_0 \mathbf{Q} : \frac{\partial \bar{\mathbf{E}}}{\partial \mathbf{E}} \quad (\text{A.12})$$

When Equation A.7 is substituted in Equation A.12 the next equation is obtained.

$$\Delta\mathbf{S} = -\rho_0 \mathbf{Q} : J^{-\frac{2}{3}} \left({}^4\mathbf{I} - \frac{1}{3} \mathbf{C} \mathbf{C}^{-1} \right) \quad (\text{A.13})$$

Adding $\Delta\mathbf{S}$ to the elastic Piola-Kirchoff stress of Equation A.8, the visco-elastic Piola-Kirchoff stress from Equation A.14 is obtained, which is the same as Equation 3.13.

$$\mathbf{S} = \rho_0 J \frac{\partial U}{\partial J} \mathbf{C}^{-1} + \rho_0 J^{-\frac{2}{3}} \frac{\partial \bar{\Psi}^0}{\partial \bar{\mathbf{E}}} : \left({}^4\mathbf{I} - \frac{1}{3} \mathbf{C} \mathbf{C}^{-1} \right) - \rho_0 J^{-\frac{2}{3}} \mathbf{Q} : \left({}^4\mathbf{I} - \frac{1}{3} \mathbf{C} \mathbf{C}^{-1} \right) \quad (\text{A.14})$$

Appendix B

Parfit

B.1 File trek_vm.c

The part of file trek_vm.c in which the equations are implemented is given here.

```
/*.....*/
void write_results(FILE *out_f)
{
    int i, inc;
    inc = rest_inc;
    for (i = 0; i < n_steps; i++) {
        inc += n_inc[i];
        time += timestep[i];
        fprintf(out_f, "%.10G %.10G %d 1 \ n %.10G \ n", labda + labdastep[i], time,
inc,
        force(timestep[i], labda, labdastep[i], n_inc[i]));
        /* fprintf(out_f, "%.10G %.10G %d 3 \ n %G \ n %G \ n %G \ n", labda + labdastep[i],
time, inc,
        force(timestep[i], labda, labdastep[i], n_inc[i]), sigtest, s2pktest);
    */
        labda += labdastep[i];
    }
    rest_inc = inc;
}
/*.....*/
double force(double dtime, double labda0, double dlabda, int incs)
{
    int i, j, k;
    double labda, dt, dl, def[3], c[3], cinv[3], c2[3], j1, j2, dj1de_dd[3], dj2de_dd[3],
dpsi0dj1, dpsi0dj2, dpsi0de_dd[3], *dpsinde_dd[3], *dqndd[3], qnsum[3],
trqnsumc, sdev[3], sigmadev[3], p, sigma[3], forc;
    labda = labda0;
    dt = dtime / incs;
```

```
dl = dlabda / incs;
if (n_visco > 0) for (i = 0; i < 3; i++) {
dpsinde_dd[i] = (double *) calloc((size_t) n_visco, (size_t) sizeof(double));
dqn_dd[i] = (double *) calloc((size_t) n_visco, (size_t) sizeof(double));
}
for (k = 0; k < incs; k++) {
labda += dl;
def[0] = labda;
if (!plane_type)
def[1] = def[2] = 1.0 / sqrt(labda);
else {
def[1] = 1.0;
def[2] = 1.0 / labda;
}
for (i = 0; i < 3; i++) {
c[i] = def[i] * def[i];
cinv[i] = 1.0 / c[i];
c2[i] = c[i] * c[i];
}
j1 = c[0] + c[1] + c[2];
j2 = (j1 * j1 - (c2[0] + c2[1] + c2[2])) / 2.0;
for (i = 0; i < 3; i++) {
dj1de_dd[i] = 2.0 - 2.0 * j1 * cinv[i] / 3.0;
dj2de_dd[i] = 2.0*(j1 - c[i] - 2.0 * j2 * cinv[i] / 3.0);
}
dpsi0dj1 = C10 + C11 * (j2 - 3.0) + 2.0 * C20 * (j1 - 3.0)
+ 3.0 * C30 * (j1 - 3.0) * (j1 - 3.0);
dpsi0dj2 = C01 + C11 * (j1 - 3.0);
for (i = 0; i < 3; i++)
dpsi0de_dd[i] = dpsi0dj1 * dj1de_dd[i] + dpsi0dj2 * dj2de_dd[i];
if (n_visco > 0) for (i = 0; i < 3; i++)
for (j = 0; j < n_visco; j++) {
dpsinde_dd[i][j] = efmult[j] * dpsi0de_dd[i];
dqn_dd[i][j] = (- qn[i][j] + dpsinde_dd[i][j]) * dt / reltime[j];
qn[i][j] += dqn_dd[i][j];
}
}
for (i = 0; i < 3; i++) {
qnsum[i] = 0.0;
for (j = 0; j < n_visco; j++) qnsum[i] += qn[i][j];
}
trqnsumc = 0.0;
if (n_visco > 0) trqnsumc = qnsum[0] * c[0] + qnsum[1] * c[1] + qnsum[2] * c[2];
for (i = 0; i < 3; i++) {
sdev[i] = dpsi0de_dd[i] - (qnsum[i] - trqnsumc * cinv[i] / 3.0);
sigmadev[i] = sdev[i] * c[i];
}
}
```

```
p = - sigmadev[2];
for (i = 0; i < 3; i++) sigma[i] = p + sigmadev[i];
forc = sigma[0] * area0 / def[0];
/*.....*/
sigtest=sigma[0];s2pkttest=sigtest/c[0];
/*.....*/
if (n_visco > 0) for (i = 0; i < 3; i++) {
free((void *) dpsinde_dd[i]);
free((void *) dqn_dd[i]);
}
return(forc);
}
/*.....*/
```